An investigation into the chemistry of HONO in the marine boundary layer at Tudor Hill Marine Atmospheric Observatory in Bermuda

Yuting Zhu[1], Youfeng Wang[1,2], Xianliang Zhou[1,3], Yasin F. Elshorbany[4], Chunxiang Ye[2],
Matthew Hayden[5], Andrew J. Peters[5]

1. Wadsworth Center, New York State Department of Health, Albany, NY, United States

2. State Key Laboratory of Environmental Simulation and Pollution Control, College of Environmental Sciences and Engineering, Peking University, Beijing, China

3. Department of Environmental Health Sciences, University at Albany, State University of New York, NY, United States

4. Atmospheric Chemistry and Climate Laboratory, College of Arts & Sciences, University of South Florida, St. Petersburg, FL, United States

5. Bermuda Institute of Ocean Sciences, St George's, Bermuda

Correspondence to: Yuting Zhu (yzhu@syr.edu) and Xianliang Zhou (xianliang.zhou@health.ny.gov)

Abstract

Here we present measurement results of temporal distributions of nitrous acid (HONO) along with several chemical and meteorological parameters during the spring and the late summer of 2019 at Tudor Hill Marine Atmospheric Observatory in Bermuda. Large temporal variations in HONO concentration were controlled by several factors including local pollutant emissions, air mass interaction with the island, and long-range atmospheric transport of HONO precursors. In polluted plumes emitted from local traffic, power plant and cruise ship emissions, HONO and nitrogen oxides (NO_x) existed at substantial levels (up to 278 pptv and 48 ppbv, respectively) and NO_x-related reactions played dominant roles in daytime formation of HONO. The lowest concentration of HONO was observed in marine air, with median concentrations at ~3 pptv around solar noon and <1 pptv during the nighttime. Considerably higher levels of HONO were observed during the day in the low-NO_x island-influenced air ($[NO_2]$ < 1 ppbv), with a median HONO concentration of ~17 pptv. HONO mixing ratios exhibited distinct diurnal cycles that peaked around solar noon and were lowest before sunrise, indicating the importance of photochemical processes for HONO formation. In clean marine air, NO_x-related reactions contribute to ~21% of the daytime HONO source and the photolysis of particulate nitrate (pNO_3) can account for the missing source assuming a moderate enhancement factor of 29 relative to gaseous nitric acid photolysis. In low-NO_x island-influenced air, the contribution from both NO_x-related reactions and pNO_3 photolysis account for only ~48% of the daytime HONO production, and the photochemical processes on surfaces of the island, such as the photolysis of nitric acid on the forest canopy, might contribute significantly to the daytime HONO production. The concentrations of HONO, NO_x and pNO_3 were lower when the site was dominated by the aged marine air in the summer and were higher when the site was dominated by North American air in the spring, reflecting the effects of long-range transport on the reactive nitrogen chemistry in the background marine environments.

1 Introduction

Nitrous acid (HONO) is a reactive nitrogen species that plays an important role in the oxidation capacity of the troposphere, as its rapid photolysis (R1) can account for a significant fraction of the production of hydroxyl radical (OH) (Elshorbany et al., 2010, 2012; Kleffmann et al., 2005; Perner and Platt, 1979):

$$HONO \xrightarrow{h\nu} NO + OH \qquad\qquad\qquad\qquad (R1)$$

The chemistry of HONO, especially during the daytime, is not well understood. Known HONO sources include direct emissions (Li, Y. et al., 2008; Oswald et al., 2013; Su et al., 2011; Trentmann et al., 2003), reactions between nitrogen oxide (NO) and OH (Zabarnick, 1993), heterogeneous production from nitrogen dioxide (NO_2) (Kleffmann, 2007), and the photolysis of nitrate on surfaces (Ye et al., 2016a; Zhou et al., 2003) or in the aerosol phase (Ye et al., 2017a, 2017b):

$$NO + OH + M \rightarrow HONO + M \qquad\qquad\qquad (R2)$$

$$NO_2 + H_2O, organics \xrightarrow{surface} \xrightarrow{h\nu} HONO \qquad\qquad (R3)$$

$$HNO_3(s) + H_2O, organics \xrightarrow{h\nu} HONO + NO_x \qquad\qquad (R4)$$

$$pNO_3(s) \xrightarrow{h\nu} HONO + NO_x \qquad\qquad\qquad\qquad (R5)$$
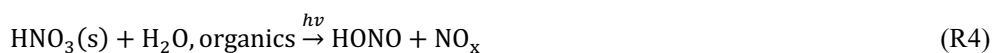
Recent field observations reported that HONO exists at considerable levels during the day, up to several parts-per-billion volume (ppbv) in the urban atmosphere (e.g., Acker et al., 2006a; Elshorbany et al., 2009) and up to several hundred parts-per-trillion volume (pptv) in the rural and remote atmosphere (He et al., 2006; Ye et al., 2016b; Zhang et al., 2009). During the daytime, HONO is removed rapidly by its photolysis, with short photolytic lifetime of ~10 min at noon under clear-sky conditions (Elshorbany et al., 2009; Kleffmann et al., 2003; Zhang et al., 2009). To sustain the observed HONO concentration against the major photochemical loss of HONO, active daytime productions are needed to explain its observed mixing ratios (Neftel et al., 1996; Zhou et al., 2001, 2002).

In the urban environment, direct HONO emission only accounts for a small fraction of its observed atmospheric concentration (Kleffmann, 2007). It is commonly believed that HONO is mainly formed by the gas-phase reactions between NO and OH (Elshorbany et al., 2010; Villena et al., 2011a) and heterogeneous reactions of NO_2 (Finlayson-Pitts et al., 2003; Kleffmann, 2007). The heterogeneous reactions leading to HONO formation occur on a variety of surfaces, including aerosol, soot, vegetation, and urban surfaces (He et al., 2006; Kleffmann et al., 1999; Ramazan et al., 2004; Reisinger, 2000; Stutz et al., 2002). It was also suggested that HONO formations are likely enhanced by solar irradiation, since measurement studies observed unexpectedly high HONO concentrations during the daytime in various environments (Acker et al., 2006b; Kleffmann et al., 2005; Vogel et al., 2003; Liu et al., 2019). One possible explanation was that organic matter serves as photosensitizer and results in light-initiated enhancement of HONO formation during the heterogeneous reaction of NO_2 (George et al., 2005; Stemmler et al., 2006, 2007). Other proposed mechanisms for HONO production

75   include gas-phase reactions of excited NO_2 with water (Li, S. et al., 2008) and the reactions between NO_2 and the hydroperoxyl-water complex ($HO_2 \cdot H_2O$) (Li et al., 2014); recent model calculations suggested that these newly proposed, NO_2-related mechanisms are likely insignificant as HONO precursors (Carr et al., 2009; Wong et al., 2011; Ye et al., 2015).

In atmospheric environments with relatively low abundance of NO_x ($NO_x = NO + NO_2$), studies proposed that
80   rapid photolysis of HNO_3 on various surfaces as well as particulate nitrate (pNO_3) photolysis might serve as important HONO sources (Ye et al., 2016b; Zhou et al., 2003, 2011)). Direct evidence from laboratory photochemistry experiment showed that there exist major photolytic rate enhancements of HNO_3 on various surfaces (Ye et al., 2016a; Zhou et al., 2003) and in aerosol sample collected from various air masses, including boundary layer air above the Atlantic Ocean and over the terrestrial environments over the United States (Ye et
85   al., 2017b, 2018). Reported pNO_3 photolytic rate constant ($J^N_{pNO_3}$, normalized by solar irradiation at tropical noontime) was higher than the rate constant for gaseous nitric acid photolysis by ~1–3 orders of magnitude (Ye et al., 2017b, 2018).

To date, few studies have investigated HONO distribution and its chemical cycling in the marine boundary layer (MBL), even though the oceans cover >70% of the earth surface (Crilley et al., 2021; Kasibhatla et al., 2018;
90   Reed et al., 2017; Wojtal et al., 2011; Ye et al., 2016b; Zha et al., 2014). Several studies observed substantial HONO concentrations (~ 3.5–11 pptv) during the day in clean, well-aged marine air (Crilley et al., 2021; Kasibhatla et al., 2018; Reed et al., 2017; Ye et al., 2016b). Evidences from both field observations and laboratory experiments suggested that pNO_3 photolysis might contribute to a major fraction of the observed level of HONO in marine atmosphere (Ye et al., 2016b). However, major uncertainties persist in current model
95   evaluations for the impact of pNO_3 photochemistry on reactive nitrogen cycling in the MBL, due to the paucity of field measurements as well as laboratory experiments that determined $J^N_{pNO_3}$ in marine aerosol samples. Additionally, the role of the ocean surface in regulating HONO cycling in the MBL remains unclear. Ocean surface is expected as a HONO sink due to its high solubility in alkaline aqueous solutions. However, several studies reported nighttime accumulation of HONO in the MBL, with higher NO_2 to HONO conversion rate in air
100   masses that have passed over the ocean surface than those that have passed over the terrestrial surface (Wojtal et al., 2011; Zha et al., 2014). It is possible that there exists an unknown HONO source at the air-sea interface; further evidence in the field and the laboratory is required to confirm this potential HONO source.

During the spring and late summer of 2019, we conducted extensive field measurements to determine the temporal distributions of HONO and the relevant parameters including NO_x, pNO_3, HNO_3, aerosol loading, O_3,
105   and meteorological parameters, at Tudor Hill Marine Atmospheric Observatory (THMAO) in Bermuda. To examine the importance of pNO_3 as photolytic HONO source, we collected aerosol samples during the field campaigns and conducted photochemistry experiments to determine the pNO_3 photolysis rate constants leading to HONO formation in the gas phase. In the present study, we present results from both field observations and laboratory experiments and discuss the chemistry of HONO as well as other reactive nitrogen species in the
110   marine atmosphere in Bermuda.

2 Experimental

2.1 Field Observations

Two intensive field studies were conducted at the THMAO site in Bermuda during the spring (April 17 – May 13) and late summer (August 16 – September 10) of 2019. The site is located on the western coast of Bermuda (32° 19' N, 64° 45' W) (Fig. S1). The sampling site is equipped with three trailers for in-house measurements and an aluminum sampling tower that is 23 m above the ground and 53 m above the sea level.

Ambient HONO concentrations were continuously measured employing a long-path absorption photometry (LPAP) system. HONO was collected in a 10-turn glass coil sampler with purified water (18.2 MΩ cm) that was obtained from a Barnstead Nanopure Diamond™ water purification system (Thermo Scientific). The collected nitrite was derivatized with a reagent solution with 5 mM sulfanilamide (SA), 0.5 mM N-(1-Naphthyl) ethylenediamine (NED) and 40 mM hydrochloric acid (HCl). The formed azo dye was detected at 540 nm using a four-channel optic fiber spectrometer (LEDspec, World Precision Instruments) with a 1-m liquid waveguide capillary cell (World Precision Instruments). To minimize potential artifact for HONO measurements on the sampling inlet wall, the HONO measurement system was installed directly on the platform of the sampling tower. The sampling assembly consisted of a coil sampler, a 3-way Teflon solenoid valve, and a Na_2CO_3 denuder. Background correction was conducted using the "zero-HONO/HNO_3" air that was generated by pulling ambient air through the Na_2CO_3 denuder. The LPAP system ran 60 min alternating cycles; during each cycle the solenoid valve feeds the coil sampler with "zero-HONO/HNO_3" air for 10 min and ambient air for 50 min. The absorbance signal was recorded in every 5 sec; data were averaged in every 10 minutes for further analyses. The LPAP system has successfully proven its effectiveness and accuracy in HONO measurement during the previous NOMADSS field data, and the reader is referred to Ye et al. (2016b, 2018) for detailed discussion for method validation and interference elimination. Briefly, interference species NO_x, peroxylacetyl nitrate (PAN) and particulate nitrite are expected to pass through the Na_2CO_3 denuder and therefore was subtracted from the ambient HONO signals. Interference from peroxynitric acid (HO_2NO_2) is expected to be negligible due to the low steady-state concentration at warm temperature (i.e., > 20 °C). Air sampling rate was 3 L min^{-1}. Detection limit of HONO was calculated as three times of standard deviation (3σ) for baseline signal and was ~0.6 pptv at 10-min time resolution.

Ambient HNO_3 and pNO_3 was measured by LPAP systems similar to that for HONO and were installed directly on the platform of the sampling tower. Gaseous HNO_3 and HONO was collected in a 10-turn glass coil sampler with purified water, the collected nitrate was converted into nitrite by passing through a Cd column in NH_4Cl buffer solution. "zero-HONO/ HNO_3" air was generated by pulling ambient air through a Na_2CO_3 denuder. HONO concentration measured by the first LPAP system was used to calculate the absorption signal contributed by HONO, which was subtracted from the total absorption signal to obtain the final product for HNO_3 concentration. Air sampling rate was 2 L min^{-1}. Detection limit of HNO_3 was ~2 pptv (3σ) at 10-min time resolution. Aerosol nitrate was scrubbed from ambient air in a continuously wetted frit-disc sampler with purified water. Collected nitrate was converted into nitrite by passing through a Cd column in NH_4Cl buffer

solution. A Na_2CO_3 denuder was installed right before the frit-disc sampler to remove all the gaseous acidic species, including HNO_3 and HONO. "Zero-pNO_3" air was generated by pumping ambient air through a 0.45-μm Teflon filter (Sartorius Biolab Products, 47 mm diameter) to generate the baseline for pNO_3 measurement. Air sampling rate was 2 L min^{-1}. Detection limit of particulate nitrate measured by the LPAP system (pNO_3^{LPAP}) was ~17 pptv (3σ) at 10-min time resolution. We corrected pNO_3^{LPAP} concentrations by multiplying with a factor of 2.06, after comparing the data with the aerosol nitrate concentrations determined in bulk aerosol samples (pNO_3^{filter}, see Sect. 2.2 for details). The correction factor was the slope of the linear correlation between the concentrations of pNO_3^{LPAP} and pNO_3^{filter} that were measured simultaneously. The discrepancy might in part result from loss of aerosol particles within the sampling compartment of the LPAP system (e.g., deposition on the walls of the Na_2CO_3 denuder) before the aerosol samples were scrubbed in the wetted frit-disc sampler. After the correction factor was applied, good agreements were achieved when comparing the temporal trends of particulate nitrate concentrations determined by the two different methods (Fig. 1).

NO_x concentrations were measured by low-level commercial chemiluminescence analyzer (Thermo Environmental Instruments Inc. 42C-TL) with a blue-light NO_2 to NO convertor (Droplet Measurement Technologies); detection limit (3σ) was ~88 and 30 pptv for NO_2 and NO, respectively at 10-min resolution. Measurement data from the NO_x analyzer meet our needs in general examination of temporal data variations that were largely influenced by pollution episodes (see Sect. 3.1 and 3.2). However, NO_x levels in relatively clean marine air were near or lower than the detection limits of the NO_x analyzer. Therefore, data obtained by the NO_x analyzer were not applicable in advanced data analyses (see Sect. 3.3 and 3.4), especially in clean marine air. During the summer field campaign, we installed a NO_2 measurement system employing LPAP technique (NO_2-LPAP). The NO_2-LPAP system was assembled following Villena et al., (2011b). In our customized NO_2-LPAP system, ozone (O_3) was firstly removed with 0.6 g/L potassium indigotrisulfonate (Villena et al., 2011b) in a 10-turn coil sampler, the O_3-free air later passed a 50-turn coil sampler that scrubbed NO_2 with a 14g/L SA (dissolved in 2.5 M acetic acid) solution and a 0.5 g/L NED solution. Air sampling rate was 0.5 L min^{-1}. NO_2-LPAP measurements (only available in the summer field campaign) successfully lowered the detection limit (3σ) to 14 pptv at 10-min resolution. Measurement systems for NO_x, NO_2-LPAP, and O_3 were installed in the trailers; ~30-m long Teflon tubing was used to sample ambient air from the platform of the sampling tower to the in-house measurement systems. O_3 was monitored with a commercial ozone monitor (Thermo 49i) based on UV absorbance at 254 nm, and the detection limit (3σ) was 1.7 ppbv at 10-min resolution.

Aerosol loading was monitored by a commercial nephelometer (Thermo Scientific) which was installed just below the platform of the sampling tower; the nephelometer provide a detection resolution of 0.1 μg m^{-3} and a particle size range of 0.1–10 μm. The intensity of ultra-violet (UV) light was measured by an Eppley TUV radiometer (295–385 nm) that was installed on the platform of the sampling tower, the measured UV data was later combined with the tropospheric ultraviolet and visible radiative transfer model (https://www2.acom.ucar.edu/modeling/tropospheric-ultraviolet-and-visible-tuv-radiation-model) to calculate the photolysis rate constant for NO_2, HONO, HNO_3 and O_3. Photolysis rate constant calculations were

performed following Zhou et al. (2011), and the details for these calculations are presented in the Supplemental Information S1.

2.2 pNO₃ Photolysis Rate Constant Determination

Bulk aerosol samples were collected on Teflon filters (Sartorius Biolab Products, 0.45 μm pore size, 47 mm diameter) during the field campaigns. There were four sampling period during each day, from 4:00–8:00, 8:00–12:00, 12:00–16:00 and 16:00–20:00 at local time. Aerosol sampling rate was 10 L min^{-1}. The collected aerosol samples were stored in tightly capped petri dishes (Analyslide®, Pall Corporation) in a freezer until use for laboratory experiments. Upon usage, each filter was cut into to two equal halves. One half of the aerosol filter was extracted by 5 mL purified water to determine the concentrations of pNO_3^{filter} and other ionic components (Na$^+$, Mg^{2+}, Ca^{2+}, NH$_4^+$, Cl$^-$, SO$_4^{2-}$) using a Dionex ICS 3000 Ion Chromatography System coupled with an AS14 4 mm analytical common and an AG14 4 mm guard column.

The other half filter was used in light exposure experiment to determine the production rate constant of HONO. During each photochemistry experiment, the aerosol filter was placed in a cylindrical flow reactor that was installed under a solar simulator. The cylindrical flow reactor, with 10-cm diameter and 1.5-cm depth, was made from a Teflon block with a quartz window on the top. A 300 W Cermax® Xenon lamp (Perkin Elmer) served as the light source in the solar simulator. Humidified zero air (50% RH) was used as the carrier gas that flow through the Teflon block reactor and the flow rate was 1 L min^{-1}. The amount of HONO that was produced during short-period (5 min) light exposure was determined with a LPAP system that was installed after the flow reactor. The readers are referred to the Supplemental Information S2 for detailed calculations of aerosol nitrate photolysis rate constant leading to HONO production $J^N_{pNO_3 \rightarrow HONO}$, which was normalized to light conditions during tropical summer with solar zenith angle of 0°.

3 Results and Discussion

Fig. 1 presents an overview for some chemical and meteorological parameters that were measured during the spring and late summer field campaigns of 2019, including HONO, NO$_x$, pNO_3^{LPAP}, pNO_3^{filter}, J$_{HONO}$, wind speed and wind direction. Data statistics for HONO, NO$_x$, pNO_3^{LPAP}, pNO_3^{filter} concentrations were summarized in Table 1. As shown in Fig. 1, we observed large temporal variations for the concentrations of reactive nitrogen species. These temporal variations resulted from joint influences by local pollutant emissions (see Sect. 3.1 for detailed discussion), long-range transport of air masses (see Sect. 3.2 for detailed discussion) and diurnal changes in solar radiation (see Sect. 3.3 for detailed discussion).

Table 1: Data statistics for the concentrations of HONO, NO_x, pNO_3^{LPAP}, pNO_3^{filter} during the spring (April 17 – May 13) and late summer (August 16 – September 10) of 2019 at the THMAO in Bermuda. For HONO, NO_x, pNO_3^{LPAP} concentrations, the statistical analyses were performed based on 10-min averaged data.

		HONO (pptv)	NO_x (pptv)	pNO_3^{LPAP} (pptv)	pNO_3^{filter} (pptv)
Spring	Range	<0.6 – 123	<118 – 48140	<17 – 1439	34 – 1146
	Mean	9.8	606	311	300
	SD	12	1970	227	236
	Median	5.4	186	284	219
	N	2600	3389	2116	93
Summer	Range	<0.6 – 278	<44 – 15103	<17 – 5961	33 – 585
	Mean	6.7	228	130	156
	SD	12	866	145	101
	Median	3.6	90.3	120	129
	N	3221	3283	2809	94

225
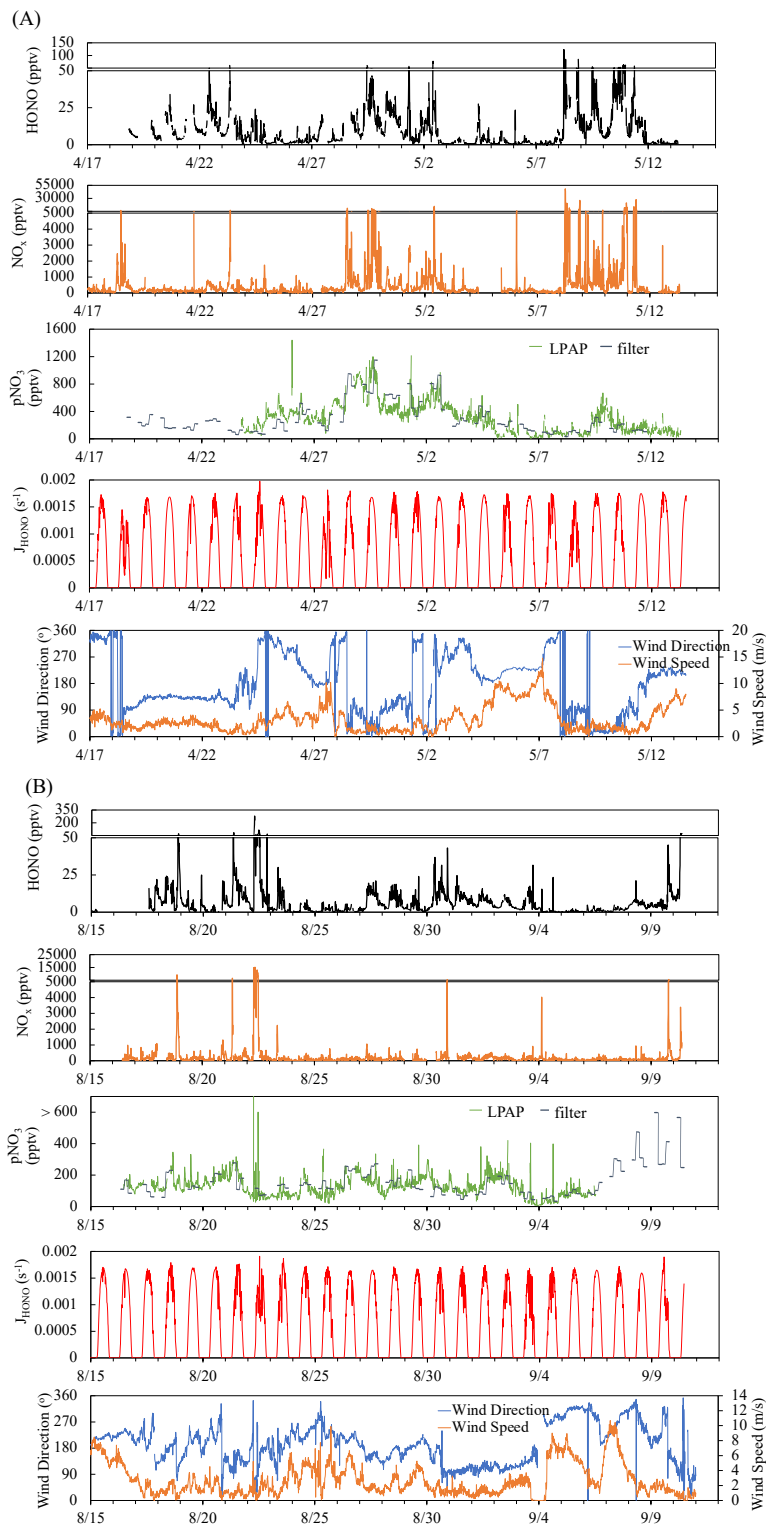
Figure 1: Time series plots of HONO, NO$_x$, pNO$_3$^{LPAP}, pNO$_3$^{filter}, HONO photolysis rate constant (J$_{HONO}$) wind direction and wind speed for the spring (A) and summer (B) field campaigns that were conducted at the THMAO in Bermuda.

3.1 Impact from local emissions

At the THMAO, reactive nitrogen measurements were quite sensitive to directions of local winds. Fig. S2 shows wind rose plots representing the distribution of wind direction and wind speed during the spring and summer field campaigns. Fig. 2 represents bivariate polar plots (generated with *openair* – an R package for air quality data analysis, Carslaw and Ropkins, 2012) showing the joint wind speed and wind direction dependences of HONO, NO_x, pNO_3^{LPAP} and HONO/NO_x ratios. When prevailing winds blew from the northwest or southwest, clean marine air with relatively low concentrations of HONO and NO_x were brought to the sampling site. It was also shown by Fig. 2 that urban and power plant plumes transported to the THMAO site with northeasterly winds. These plumes, originated from the city of Hamilton (i.e., capital city of Bermuda with busy road traffics and a nearby power plant) and the Royal Naval Dockyard (i.e., a harbor of cruise ships), contained HONO and NO_x at substantial levels (Fig. 2). The highest concentrations of HONO and NO_x reached 278 pptv and 48 ppbv, respectively. The pollution level within the plumes was comparable with that observed in polluted marine atmospheric environments at coastal sites in Hong Kong (Zha et al., 2014), on Tuoji Island in eastern Bohai Sea, China (Wen et al., 2019), and on Saturna Island in British Columbia, Canada (Wojtal et al., 2011).
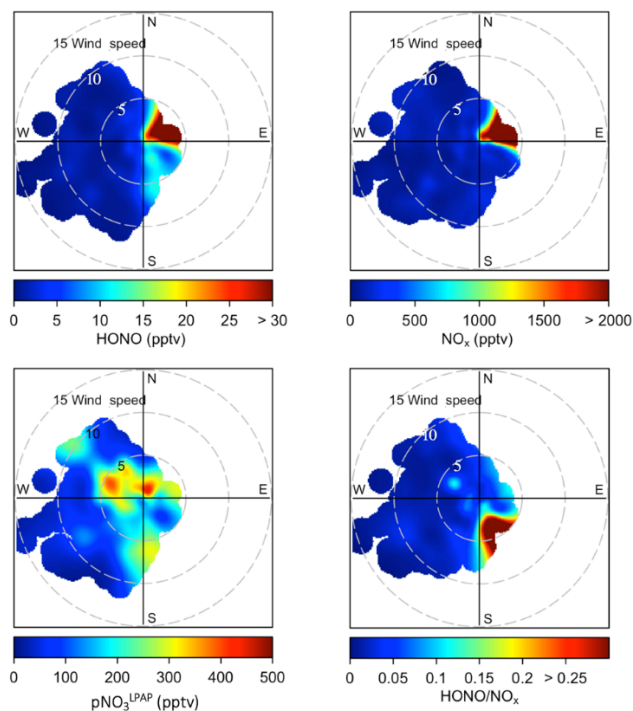
Figure 2: Bivariate polar plots showing the joint wind speed and wind direction dependences of HONO, NO_x, pNO_3^{LPAP} and HONO/NO_x ratios during the two field campaigns in Bermuda. Data measured during the spring and the summer seasons were combined to generate these polar plots. The color scales represent HONO, NO_x, pNO_3^{LPAP} concentrations, and HONO/NO_x ratios. The radial scale shows the wind speed in m/s.

Here we divided our measurement datasets into different categories based on three types of local influences: clean marine air (wind directions ranged from 210 to 330°), island-influenced air (wind directions ranged from 0 to 180°, [NO_2] < 1 ppbv) and polluted plumes (wind directions ranged from 0 to 180°, [NO_2] ≥ 1 ppbv). It should be pointed out that the clean marine air was still affected by ship emissions, and thus spikes were removed from the data set when averaging HONO and NO_2 concentration in clean marine air to eliminate influences of emissions from passing ships. Average NO_2 and HONO concentrations within the removed spikes were 1563 pptv and 15 pptv, respectively. Whisker plots comparing HONO, NO_x, pNO_3^{LPAP} concentrations and HONO/NO_x ratios under different types of local influences were presented in Fig. 3. HONO and NO_x concentrations in polluted plumes were higher than those in marine by ~1–3 orders of magnitude. The relative contribution from direct emissions to the high-level HONO may be substantial during the night or under low-light conditions, but is expected to be relatively small within 4 hours before and after solar noon. Estimated transport times from the city of Hamilton to the THMAO site were ≥ 1.4 h (with ~10 km distance and ~2 m/s wind speed) and were several times longer than the HONO photolytic lifetime (~10–18 min under clear skies) from 9:30 to 17:30 during the day. Therefore, the observed HONO in the daytime plumes at the site was mostly produced during the air transport from emission sources to the THMAO site via gas-phase reaction (R2), heterogeneous reactions (R3) on aerosol and island surfaces, and maybe some other chemical sources.

The island-influenced air was the marine air mass that passed over less populated regions of the island and was thus not significantly impacted by anthropogenic emissions. The concentrations of HONO and NO_x were higher in island-influenced air than in clean marine air (Fig. 3). It was also observed that the highest HONO/NO_x ratios (an indicator for the efficiency of HONO production) were found in island-influenced air. The underlying mechanism for this active HONO production is unknown. One possible explanation is that reactions occurring on various surfaces (e.g., the ground and vegetation surfaces) of the island contribute significantly to HONO production during the day (see Sect. 3.4 for detailed discussion).
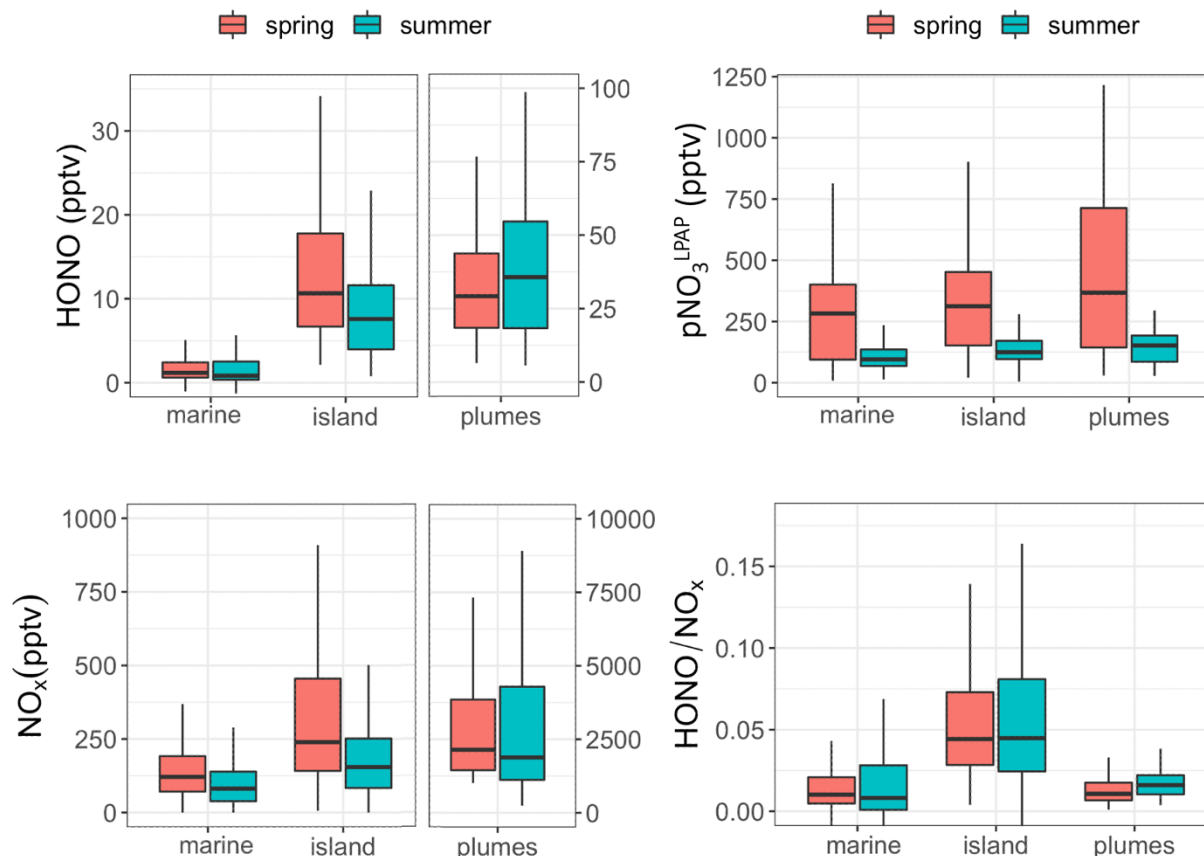
Figure 3: Whisker plots comparing of HONO, NO_x, pNO$_3$^LPAP concentrations and HONO/NO_x ratios in clean marine air, island-influenced air, and polluted plumes during the spring and the summer field campaigns in Bermuda. The thick lines represent median values, the boxes the 25th and 75th percentiles, and the whiskers the largest value within 1.5 times interquartile range above 75th percentile and the smallest value within 1.5 times interquartile range below 25th percentile.

Fig. 3 also shows that local wind direction did not appear as a significant factor controlling pNO$_3$ concentrations. It is concluded that pNO$_3$ concentration was mainly controlled by the origins of the air masses and long-range transport (see Sect. 3.2) and was relatively independent from the impacts by local pollution emissions.

3.2 Impact from long-range transport

The THMAO, located on the western coast of the Bermuda island, is influenced by air masses that originated from different source regions (Moody and Galloway, 1988; Todd et al., 2003). Fig. S3 shows a summary of the 7-day backward trajectories; the trajectories were calculated daily starting at local noontime using NOAA'S HYSPLIT model (https://www.ready.noaa.gov). In the spring season, 23 out of 27 of the daily trajectories indicated northwesterly flows that originated from the North American continent. Exceptions were found from

May 3 to May 7 when the sampling site received aged marine air. In the summer season, the site was under the influence of the Bermuda high and received well-aged marine air above the Atlantic Ocean. On September 7, the Bermuda high was disturbed as hurricane Dorian traveled along the eastern coast of the US. Calculated backward trajectories indicated fast-traveling air flows originated on the North American continent during September 7–10.

In order to provide direct comparisons of data based on source regions of air masses, i.e., North American (NA) in the spring and North Atlantic Ocean (NAO) in the summer, we excluded measurement data collected during May 3–7 and September 7–10, and generated whisker plots (Fig. S4) comparing HONO, NO_x, pNO_3^{LPAP} concentrations and HONO/NO_x ratios. The plots in Figs. 3 and S4 are almost identical, due to the fact that most of the air masses originated from North America in spring but circulated above the North Atlantic Ocean during the summer. It appears that the local emission and the island modification of the air masses controlled the levels of HONO, NO_x and the HONO/NO_x ratio. However, the level of pNO_3 was significantly higher in NA than in NAO as a result of long-distance transport of this species and was less dependent on how the air masses interacting with the island. For HONO production efficiencies, no significant differences were found in the HONO/NO_x ratios between the two air mass categories (Fig. S4) under each type of local influences, as expected from HONO being a short-lived species controlled by in-situ production and rapid loss (Elshorbany et al., 2009; Kleffmann et al., 2003; Zhang et al., 2009; Zhou et al., 2001, 2002). However, it should be noted that long-distance traveled air flows could affect HONO chemistry under certain circumstances. In fact, significant changes in reactive nitrogen chemistry were observed on 9/7–9/8 while aged North Atlantic air was replaced by a fast-traveling flow from the Northeastern US. The readers are referred to Sect. 3.5 for detailed discussions.

3.3 Diurnal variations

Diurnal cycles for HONO, NO_2, pNO_3^{LPAP} concentrations and HONO/NO_2 ratios in marine and island-influenced air are presented in Fig. 4 after binning measurement data into 1 h intervals. Urban plumes represented high-NO_x air that were emitted from point sources (e.g., power plant emission) or mobile sources (e.g., road traffic emissions). Diurnal trends in polluted plumes are not shown in Fig. 4 because (1) temporal variability of reactive nitrogen species in polluted plumes was largely dependent on the source of the pollutant emission and (2) data collected in polluted plumes are insufficient to represent diurnal cycles for a 24-h time period.
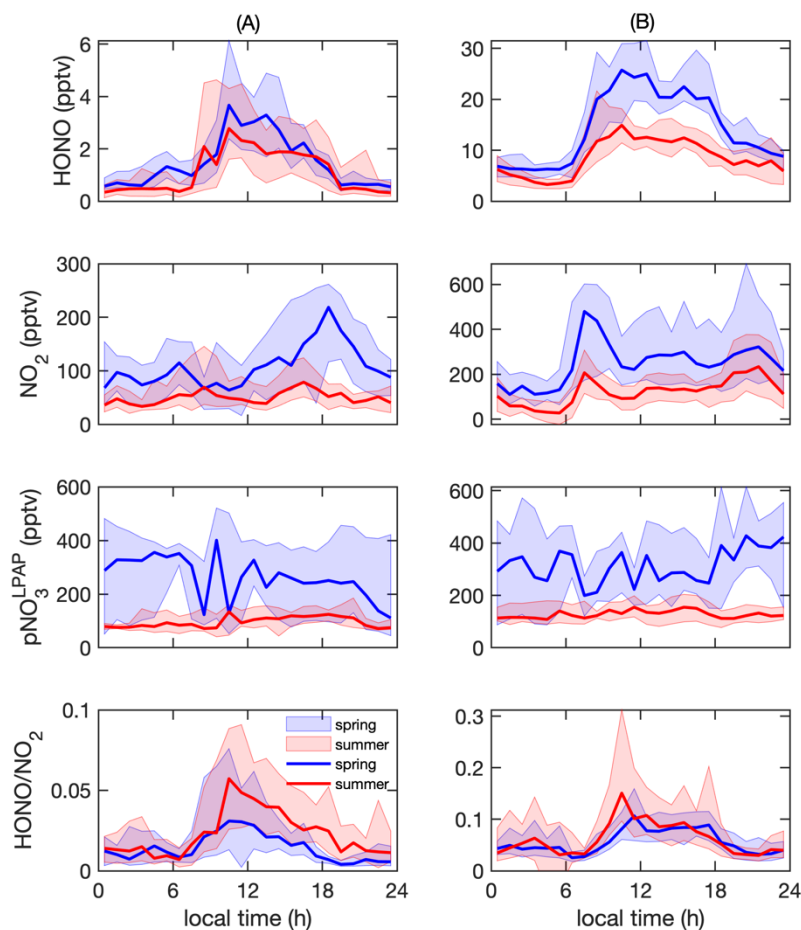
Figure 4: Diurnal profiles of HONO (pptv), NO₂ (pptv), $\underline{pNO_3^{LPAP}}$ (pptv), and HONO/NO₂ ratio in (A) clean marine air and (B) island-influenced air. The solid lines represent the median values and the areas represent 25th to 75th percentiles.

HONO concentrations exhibited distinct diurnal cycles in clean marine air (Fig. 4A), with maxima of ~3 pptv around solar noon and minima near or below ~1 pptv during the early morning hours before sunrise. The observed diurnal trends of HONO were in good agreement with those observed from Cape Verde Atmospheric Observatory located in the tropical Atlantic boundary layer (Crilley et al., 2021; Kasibhatla et al., 2018; Reed et al., 2017; Ye et al., 2017a). At night, HONO concentrations reached steady state concentrations of ~1 and 0.7 pptv for the spring and summer season, respectively; this nocturnal HONO concentration steady-states were consistent with previous reports in clean marine boundary layer (Crilley et al., 2021; Kasibhatla et al., 2018; Reed et al., 2017; Ye et al., 2017a). In island-influenced air, HONO concentrations also exhibited diurnal cycles representing higher concentrations during the daytime than the nighttime. The observed diurnal cycles confirmed that HONO cycling is controlled by local photoproduction and rapid photolytic loss (Elshorbany et

al., 2009; Kleffmann et al., 2003; Zhang et al., 2009; Zhou et al., 2001, 2002). During the summer season, median value for noontime maxima of HONO concentrations was ~13 pptv and was significantly lower than the median daytime maxima of ~23 pptv for the spring season. This seasonal difference in HONO daytime maxima

340   likely resulted from the low "background" levels of HONO daytime precursors including NO_x and pNO_3 in aged marine air that dominated our summer field campaign, as discussed in Sect. 3.2.

The concentrations of NO_2 were generally higher during the day than during the night, but with a bimodal distribution pattern that peaks in the morning and the evening hours (Fig. 4), which is different from a previously reported monomodal pattern of NO_2 that peaked around solar noon (Reed et al., 2017; Ye et al.,

345   2017a). This bimodal distribution pattern, which was more distinct in island-influenced air than in marine air and also more distinct in spring than in summer, were likely due to the increases in marine traffic and sporting boat activity in the waters off Bermuda western shore during the westerly air flow; the observed NO_2 peaks coincided with the local morning and evening traffic rush hours during the island-influenced periods, with a possible 1–2 hour transport time delay from more populated areas. It is interesting to point out that the patterns

350   of HONO and NO_2 were highly different during the day, suggesting that NO_2 was unlikely a major HONO precursor in the background air masses when NO_x was below 1 ppbv.

pNO_3 is known as another important HONO precursor (Ye et al., 2016b, 2017b, 2018). In both clean marine air and island-influenced air, we observed significant seasonality and no clear diurnal cycles regarding pNO_3 concentrations, confirming the importance of long-range transport contribution to pNO_3 concentrations, as

355   discussed in Sect. 3.2.

The plateaus of HONO concentration and HONO/NO_2 ratio consistently occurred in the daytime around solar noon (±3 h) under all types of local influences, indicating the existence of active daytime photochemical HONO sources to compensate the rapid photolytic loss of HONO (Oswald et al., 2015; Zhou et al., 2007). The daytime HONO/NO_2 ratios were ~0.04 and 0.10 in clean marine air and island-influenced air, respectively. The

360   significantly higher HONO/NO_2 ratios in island-influenced air is indicative of a significant contribution of HONO by heterogeneous processes occurring on island surfaces. The readers are referred to Sect. 3.4 for detailed discussion regarding factors that affected the daytime chemistry of HONO.

During the nighttime, we observed pseudo steady-state concentrations of HONO in the marine atmosphere (Fig. 4). Nighttime steady states in HONO concentrations were previously reported in clean (Crilley et al., 2021;

365   Kasibhatla et al., 2018; Reed et al., 2017; Ye et al., 2017a) and polluted marine environment (Wojtal et al., 2011). Several recent research works showed nighttime HONO accumulations in polluted marine environments (Wen et al., 2019; Wojtal et al., 2011; Yang et al., 2021; Zha et al., 2014). With higher NO_2-to-HONO conversion rates and higher HONO/NO_2 ratios in the air masses passing over sea surface than land surface (Zha et al., 2014), the NO_2 heterogeneous reaction on the sea surface microlayer has been proposed to be the

370   nighttime HONO source in the nocturnal polluted MBL. However, we did not observe any nighttime HONO accumulation in the MBL at THMAO site in either clean marine air or the island-influenced air. Furthermore, the HONO/NO_2 ratios were lower in the clean marine air (<0.02) than in the island-influenced air (<0.06),

contradicting the earlier reports. The lack of nighttime HONO accumulation and the significantly lower HONO concentrations and HONO/NO₂ ratio during the night than the day suggest the existence of a nighttime HONO sink in the absence of its photolytic loss, i.e., the dry deposition of HONO onto ocean surface. It is therefore concluded that ocean surface is a net HONO sink in the clean MBL.

Island-influenced air was a marine air mass that interacted with the land surfaces during its transit over the island before reaching the sampling site. The interaction time between the air mass and the island surface was in the range from less than one hour to several hours, depending on the wind flow direction. Higher pseudo steady-state HONO concentration was quickly reached during the day (Fig. 4) due to its strong photochemical source and fast photolytic loss. During the night, enhanced HONO accumulation from NO₂ heterogeneous reactions on island surfaces occurred only during the relatively short time when the air mass was over the island. As a result, the nighttime HONO concentration and HONO/NO₂ ratio in the island-influenced air would remain low but would be higher than that in the clean marine air (Fig. 4).

3.4 Daytime HONO budget

In the current section, we examine daytime HONO budget, equation (1), using the data obtained during the day around solar noon, from 10:00 to 15:00 local time.

$$\frac{d[HONO]}{dt} = P_{HONO} - L_{HONO} \tag{1}$$

where P_{HONO} and L_{HONO} are the overall HONO production and loss rates (in pptv·s⁻¹), respectively. During the daytime, known HONO daytime formation sources (Elshorbany et al., 2010; Finlayson-Pitts et al., 2003; Ye et al., 2016b; Zhou et al., 2003) include NOₓ-related reactions (R2, R3) ($P_{NO_x \rightarrow HONO}$), the photolysis of HNO₃ on surfaces (R4) ($P_{HNO_{3(ads)} \rightarrow HONO}$) and the photolysis of pNO₃ (R5) ($P_{pNO_3 \rightarrow HONO}$):

$$P_{HONO} = P_{NO_x \rightarrow HONO} + P_{pNO_3 \rightarrow HONO} + P_{HNO_{3(ads)} \rightarrow HONO} + P_{other} \tag{2}$$

where P_{other} represents other unaccounted processes.

HONO photolysis ($L_{photolysis}$) is the dominant HONO sink during the day. Minor HONO sinks include its reaction with OH ($L_{HONO+OH}$) and its dry deposition ($L_{deposition}$):

$$L_{HONO} = L_{photolysis} + L_{HONO+OH} + L_{deposition}$$

$$= [HONO] \times J_{HONO} + k_{HONO+OH} \times [HONO] \times [OH] + \frac{v_{HONO}}{H} \times [HONO] \tag{3}$$

In a daytime photo-steady state, $\frac{d[HONO]}{dt} \approx 0$:

$$P_{HONO} \approx L_{HONO} = [HONO] \times (J_{HONO} + k_{HONO+OH} \times [OH] + \frac{v_{HONO}}{H}) \tag{4}$$

J_{HONO} is the photolysis rate constant of HONO (s⁻¹). $k_{HONO+OH}$ is the constant for the reaction between HONO and OH (cm³ molecule⁻¹ s⁻¹) obtained from Atkinson et al. (2004). In this section, a constant [OH] of 6×10⁶ molecules cm⁻³ is assumed for all of our daytime budget analyses. v_{HONO} is the deposition velocity, which is set to a high value of 1 cm s⁻¹ (Harrison et al., 1996; Stutz et al., 2002), and H the vertical transport distance. The

value of H (i.e., 116 m) was calculated following Zhang et al. (2009), with an assumed turbulent diffusion coefficient K_z of 10^5 cm^2 s^{-1} and a HONO photolytic lifetime of 670 s (11 min). The medians for calculated daytime $L_{photolysis}$ are 3.8×10^{-3}, 2.4×10^{-2}, and 7.3×10^{-2} pptv·s^{-1} for clean marine air, island-influenced air, and polluted plumes, respectively. $L_{photolysis}$ is the dominant HONO sink during the day, accounting for ~92% of HONO loss rate and is ~1 order of magnitude higher than $L_{HONO+OH}$ and $L_{deposition}$. The medians for calculated daytime $L_{HONO+OH}$ are 9.1×10^{-5}, 5.8×10^{-4}, and 1.8×10^{-3} pptv·s^{-1} for clean marine air, island-influenced air, and polluted plumes, respectively. The medians for calculated daytime $L_{deposition}$ are 2.6×10^{-4}, 1.4×10^{-3}, and 4.3×10^{-3} pptv·s^{-1} for clean marine air, island-influenced air, and polluted plumes, respectively.

3.4.1 Polluted plumes

NO_x-related processes, including the gaseous reaction between NO and OH (R2) and the heterogeneous production from NO_2 (R3), were the most well-studied HONO sources during the daytime (e.g., Elshorbany et al., 2010; Finlayson-Pitts et al., 2003; He et al., 2006; Kleffmann et al., 1998; Villena et al., 2011a). However, chemical kinetics data on the relevant reactions in the MBL were scarce and thus not sufficient for quantitative analyses of HONO daytime budget. Nighttime HONO accumulation, commonly used to estimate the net NO_2 to HONO rates in marine atmospheric environments (Wen et al., 2019; Yang et al., 2021; Zha et al., 2014), was not observed in the present study (see Sect. 3.3). Therefore, we chose to evaluate the role of NO_x as daytime HONO source by examining the NO_x-HONO relationship in the high-NO_x plume where NO_x is the dominant precursor via reactions R2–R3.

425
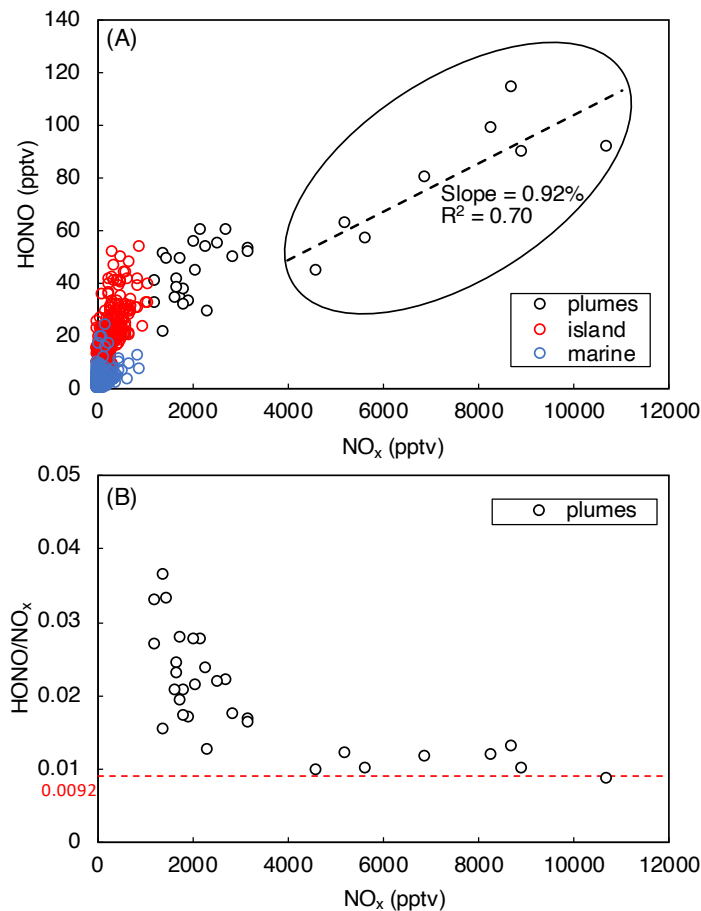
Figure 5: HONO concentrations plotted against NO_x concentration during daytime from 10:00 to 15:00. Data were divided into three categories (i.e., polluted plumes, island-influenced air, and clean marine air) based on local wind direction and NO_2 concentrations. The black dash line in panels (A) represents the best fits of linear regression between HONO and NO_x in polluted plumes (0<wind direction<180°, $[NO_x] > 4$ ppbv). The red

430   dashed lines in panel (B) indicates where HONO/NO_x= 0.0092.

Fig. 5A indicates that HONO concentration increased with $[NO_x]$, as expected from NO and NO_2 being HONO precursors. It was also shown that the HONO/NO_x ratio decreased with $[NO_x]$ (Fig. 5B) due the decreasing relative contribution from other HONO-formation mechanisms. With the increase in NO_x concentration in the

435   pollution plumes, the NO_x-related processes became the dominant HONO precursor, leading to a stabilization in the HONO/NO_x ratio at $[NO_x] >4$ ppbv (Fig. 5B). In the daytime plumes ($[NO_x] >4$ ppbv, 10:00–15:00), HONO concentrations were found to be strongly correlated with $[NO_x]$ (Slope = 0.0092, $R^2 = 0.70$), as highlighted within the black circle in Fig. 5A. The slope of 0.0092 in the [HONO]-[NO_x] plot agrees well with the stabilized HONO/NO_x ratio displayed in Fig. 5B. Constant HONO/NO_x ratio of 0.0092 was then used to estimate the

440   efficiency of HONO production through NO_x-related reactions:

$$P_{NO_x \to HONO} = 0.0092 \times [NO_x] \times (J_{HONO} + k_{HONO-OH} \times [OH] + \frac{v_{HONO}}{H}) \qquad (5)$$

The $P_{NO_x \to HONO}$ values are calculated for polluted plumes with $[NO_x] > 4$ ppbv. The median daytime $P_{NO_x \to HONO}$ value is 8.4×10^{-2} pptv·s^{-1}, which is nearly sufficient to compensate the daytime HONO loss of 9.4×10^{-2} pptv·s^{-1} within our measurement uncertainties.

In polluted plumes with $[NO_x] < 4$ ppbv, the HONO/NO$_x$ ratio increases with lowering NO$_x$ (Fig. 5B), and the calculated $P_{NO_x \to HONO}$ by equation (5) fails to fully account for the HONO production budget needed to compensate the rapid HONO loss rates, L_{HONO}. HONO production rate that is uncounted by NO$_x$-related reactions ($P_{missing}$) was calculated using the following equation:

$$P_{missing} = L_{HONO} - P_{NO_x \to HONO} \qquad (6)$$

The median $P_{missing}$ value is of 3.7×10^{-2} pptv·s^{-1} in polluted plumes with $[NO_x] < 4$ ppbv, which accounts for 56% of the median HONO production rates needed to counter HONO loss rates. The daytime missing HONO source was commonly reported by previous field studies in forested, marine, and urban environments (e.g., Elshorbany et al., 2009; Oswald et al., 2015; Su et al., 2011; Ye et al., 2016b), reflecting the source strength of HONO production from processes other than NO$_x$ reactions, such as pNO$_3$ and surface HNO$_{3(ads)}$ photolysis. In this work, budget analyses for $P_{pNO_3 \to HONO}$ and $P_{HNO_{3(ads)} \to HONO}$ were attempted for clean marine air (see section 3.4.2) and island-influenced air (see 3.4.3), not for polluted plumes, since pNO$_3$ and HNO$_{3(ads)}$ photolysis are expected to be more important as HONO precursors in low-NO$_x$ environments than high-NO$_x$ environments.

3.4.2 Clean marine air

For clean marine air coming directly over the ocean, the ocean surface is likely a net HONO sink due to high solubility of HONO in alkaline seawater. The HONO production efficiencies through NO$_x$-related processes were expected to be lower in the air mass in contact with the ocean surface than that over the island. Therefore, $P_{NO_x \to HONO}$ calculated using equation (5) is expected to overestimate HONO production rate through NO$_x$-related processes in clean marine air and the following equations are used to estimate the HONO production rates through R2 and R3:

$$P_{NO+OH \to HONO} = k_{NO+OH} \times [OH] \times [NO] \qquad (7)$$

$$P_{NO_{2(aerosol)} \to HONO} = k_{NO_2-aerosol} \times [NO_2] \qquad (8)$$

Where k_{NO+OH} is the reaction rate constant between NO and OH obtained from Atkinson et al., (2004). For equation (8), $k_{NO_2-aerosol}$ was calculated as:

$$k_{NO_2-aerosol} = \frac{1}{4} \times \overline{v_{NO_2}} \times \frac{S}{V} \times \gamma_{NO_2-aerosol} \qquad (9)$$

470   Where $\overline{v_{NO_2}}$ is the average molecular speed of NO_2, $\frac{S}{V}$ is the surface to volume ratio, and $\gamma_{aeroosl}$ is the uptake

coefficient of NO_2 on aerosol surfaces. A $\frac{S}{V}$ ratio of 5×10^{-5} m^{-1} is used, based on 20 µg·m^{-3} of 1-µm sea-salt

aerosol particles. An upper limit $\gamma_{NO_2-aerosol}$ value of 2×10^{-5} is also used, taking into account the photo-

enhancement of HONO formation through heterogeneous reaction of NO_2 (Li et al., 2010; Stemmler et al.,

2006). The calculated medians for $P_{NO+OH\rightarrow HONO}$ and $P_{NO_2(aerosol)\rightarrow HONO}$ are 8.9×10^{-4} and 5.9×10^{-6} pptv·s^{-1} in

475   clean marine air, which only account for minor fractions (21% and 0.14%, respectively) of the median HONO

production rate needed to counter HONO loss rate. $P_{NOx\rightarrow HONO}$, defined here as the sum of $P_{NO+OH\rightarrow HONO}$ and

$P_{NO_2(aerosol)\rightarrow HONO}$ is estimated to be 9.0×10^{-4} pptv·s^{-1} in clean marine air, and is lower than the 1.2×10^{-3} pptv·s^{-1}

calculated using equation (5), confirming that HONO production efficiencies through NO_x-related processes are

lower in air mass over the ocean surface than that over the island.

480   In clean marine air, ground-surface related reactions are absent, and pNO_3 might serve as an important HONO

precursor that explains its missing daytime source. Various research works, including those conducted in the

field (Ye et al., 2016b, 2018) and the laboratory (Ye et al., 2017b) reported significant enhancement in the

photolysis rate constant of particulate nitrate (J_{pNO_3}) compared to that of gaseous nitric acid (J_{HNO_3}). To date, the

largest dataset for $J_{pNO_3}^N$ was reported by Ye et al. (2017b) which included experimental results for aerosols

485   collected from various environments, including "ground" samples from rural, urban and remote mountain areas,

as well as "aloft" samples from the troposphere over the Southeastern US. For clean marine environment, Ye et

al. (2016b) reported 150–300 fold enhancement in pNO_3 photolysis relative to HNO_3 photolysis based on

experimental data for a single aerosol sample collected on an aircraft during a research flight to the Atlantic

Ocean off North and South Carolinas. However, it is possible that such high enhancement factor (EF) cannot be

490   extrapolated to a larger geographical scale (e.g., the global oceanic environments), since several reactive

nitrogen chemistry models suggested that the better approximation for reactive nitrogen cycling is achieved

when pNO_3 photolysis is assumed to be moderately enhanced (e.g., ~10–25 times higher) relative to the

photolysis of HNO_3 (Kasibhatla et al., 2018; Reed et al., 2017; Romer et al., 2018; Ye et al., 2017b). In order to

evaluate the rate of daytime HONO production from pNO_3 photolysis ($P_{pNO_3\rightarrow HONO}$) in clean marine air of

495   Bermuda, we assume it accounting for 100% of the $P_{missing}$, and calculate an upper-limit enhancement factor

for pNO_3 photolysis leading to HONO production relative to HNO_3 photolysis (EF^*):

$$EF^* = \frac{P_{missing}}{[pNO_3^{filter}]\times J_{HNO_3}} \tag{10}$$

Where J_{HNO_3} is the gaseous nitric acid photolysis rate constant and $[pNO_3^{filter}]$ is the particulate nitrate

concentration determined from the aerosol samples collected on Teflon filters. $P_{missing}$ is calculated using

500   equation (6) and $P_{NO_x\rightarrow HONO}$ is defined as the sum of $P_{NO+OH\rightarrow HONO}$ and $P_{NO_2(aerosol)\rightarrow HONO}$ in clean marine air.

The median value for $P_{missing}$ is 3.3×10^{-3} pptv·s^{-1} in clean marine air. The median value and the 25th to 75th

percentiles of the calculated EF^* are 29, 20 and 43, respectively. It should be noted that HONO is assumed as

the main product of pNO_3 photolysis here. The calculated median EF^* value agrees with several recent studies

(Kasibhatla et al., 2018; Reed et al., 2017; Romer et al., 2018; Ye et al., 2017b) that pNO$_3$ photolysis is moderately enhanced (*EF* range from 1 to 30) relative to the photolysis of HNO$_3$ in the marine environments, but is much lower than the *EF* between 150 and 300 reported by Ye et al. (2016b). The discrepancies may represent the differences in the environments encountered in these different studies, i.e., the lower MBL in this work and other previous ground-based studies (e.g., Kasibhatla et al., 2018; Reed et al., 2017) *vs* the upper marine boundary layer encountered in the aircraft study by Ye et al (2016b). Significantly higher pNO$_3$^{LPAP} concentrations were observed in marine air at the THMAO site (medians of 284 and 120 pptv in spring and summer, respectively, Table 1) than in the upper marine boundary layer (~50 pptv) (Ye et al., 2016b), with a much high pNO$_3$/HNO$_3$ ratio, ~ 6 in this work *vs* ~ 1 reported by Ye et al. (2016b). Furthermore, super-micron particles were found to dominate the aerosol size distribution at the THMAO site, reflecting the younger age of marine aerosols generated by breaking waves (Keene et al., 2007). Laboratory studies have shown that pNO$_3$ photolysis were enhanced by lower pNO$_3$ concentration, smaller aerosol particle size, and higher acidity, resulting in photolysis rate constants that varied by two orders of magnitude (Bao et al., 2018; Ye et al., 2017b).

Laboratory-based photochemistry experiments were performed to determine pNO$_3$ photolysis rate constants using aerosol samples collected on Teflon filters during the field campaigns. The determined rate constant ($J^N_{pNO_3 \rightarrow HONO}$), normalized to the tropical noontime conditions at ground level with a J_{HNO_3} of 7×10^{-7} s^{-1}, varies from 1.0×10^{-6} s^{-1} to 1.8×10^{-5} s^{-1} with a mean value (±SD) of 3.2 (±2.3) $\times 10^{-6}$ s^{-1} and a median value of 2.6×10^{-6} s^{-1}. Our experimental results indicated that HONO is the main product of pNO$_3$ photolysis; the determined average HONO:NO$_2$ molar yield is 7.5:1. The measured enhancement factor (EF^m) was calculated as:

$$EF^m = \frac{J^N_{pNO_3 \rightarrow HONO}}{7 \times 10^{-7}}$$
(11)

The EF^m value varies from 1.5 to 26, with a mean value (±SD) of 4.6 ± 3.3 and a median of 3.7. The low EF^m is similar to the recent reported *EF* values of ≤10 determined by Shi et al. (2021) for NaNO$_3$ and NH$_4$NO$_3$ particles and the *EF* range of 1–30 reported by Romer et al. (2018), but much lower than the *EF* values for ambient aerosol particles collected in filters from various environments (Bao et al., 2018; Ye et al., 2016b, 2017b). While no categorial differences in EF^m are observed for different types air masses under influences of island-modification or long-range atmospheric transport, the measured EF^m value decreases with pNO$_3$ concentration, as previously reported (Ye et al., 2017b). Furthermore, the highest EF^m values are found to be associated with air that represented high HNO$_3$/pNO$_3$ ratios, suggesting the enhancing effect of aerosol acidity, as observed by Bao et al. (2018). Additional details for the temporal variations and potential factors affecting pNO$_3$ photolysis rate constants are to be discussed in a separate manuscript (Zhu et al., in preparation).

Fig. 6 illustrates the contributions of different production and loss pathways to the chemistry of HONO from 10:00 to 15:00 in clean marine air. In Fig. 6A, the upper-limit of HONO production rate by pNO$_3$ photolysis ($P^*_{pNO_3 \rightarrow HONO}$) is 3.3×10^{-3} pptv·s^{-1}, assuming it accounts for 100% of the $P_{missing}$, and it can be calculated by equation (12) using an EF^* of 29:

$$P^*_{pNO_3 \to HONO} = 29 \times J_{HNO_3} \times [pNO_3^{filter}] \quad\quad\quad (12)$$

In Fig. 6B, the HONO production rate by pNO₃ photolysis ($P^m_{pNO_3 \to HONO}$) is estimated using EF^m:

$$P^m_{pNO_3 \to HONO} = EF^m \times J_{HNO_3} \times [pNO_3^{filter}] \quad\quad\quad (13)$$

The median of $P^m_{pNO_3 \to HONO}$ in clean marine air is 3.5×10^{-4} pptv·s^{-1}, which only accounts for 8% for the total production budget of HONO during the daytime. Other unknown HONO formation processes are needed to make up about 70% of the daytime HONO production budget in this scenario.
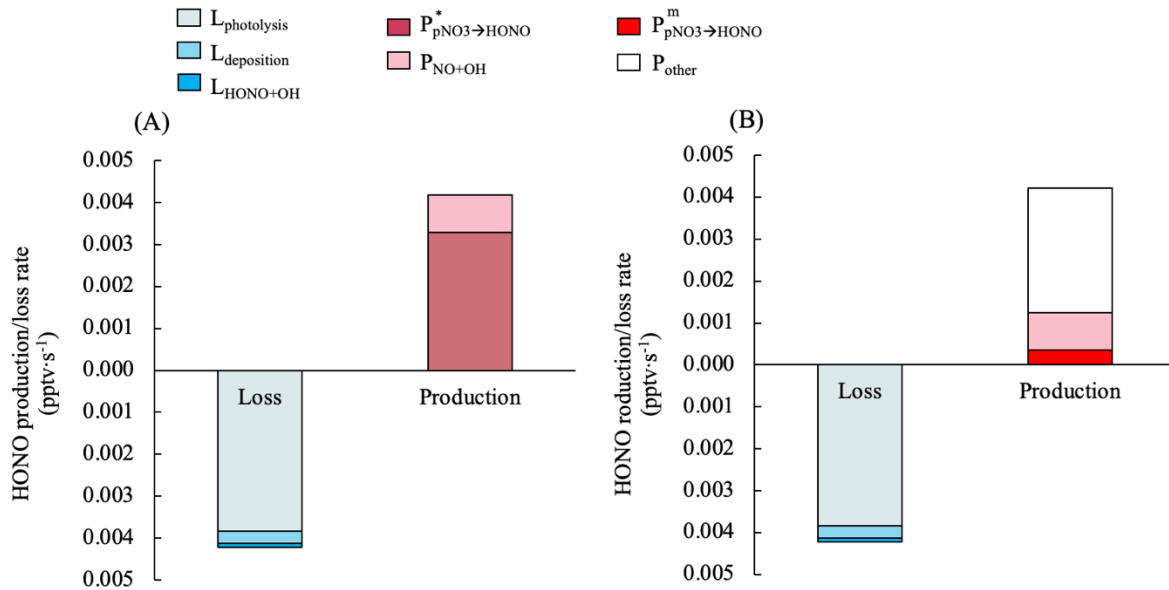
Figure 6: Median values for the production and loss rates of HONO contributed by different processes in clean marine air from 10:00 to 15:00. HONO production rate by NO₂ heterogeneous reactions on aerosols contributed to <0.2% of the HONO production budget, and therefore is not displayed in this figure. For HONO production rate via pNO₃ photolysis, $P^*_{pNO_3 \to HONO}$ in panel (A) was estimated with a constant EF^* value of 29 and $P^m_{pNO_3 \to HONO}$ in panel (B) was estimated with the measured enhancement factor EF^m.

The large discrepancy between EF^m and EF^* might result from a bias in photolysis rate constants determined in the laboratory using stored marine aerosol samples collected on Teflon filters. The sampling and storage may alter the physical and chemical properties of the sea-salt aerosols, such as aggregation of particles and deprotonation of nitrate, resulting in the lower nitrate photo-reactivity compared to pNO₃ in the ambient aerosol particles in real marine atmospheric environment. Therefore, while $P^*_{pNO_3 \to HONO}$ calculated using EF^* and $P^m_{pNO_3 \to HONO}$ calculated using EF^m should be considered as the upper-limit and the lower-limit estimates for HONO production rates by pNO₃ photolysis, respectively.

3.4.3 Island-influenced air

For island-influenced air, we identified a large extra daytime HONO source (P_{extra}) that are not accounted for by the combined sources of $P_{NO+OH\rightarrow HONO}$, $P_{NO_2(aerosol)\rightarrow HONO}$, and $P^*_{pNO_3\rightarrow HONO}$ via equation (7), (8) and (12), respectively. The calculated medians for $P_{NO+OH\rightarrow HONO}$, $P_{NO_2(aerosol)\rightarrow HONO}$, and $P^*_{pNO_3\rightarrow HONO}$ in island-influenced air are 2.6×10^{-3} pptv·s^{-1}, 2.0×10^{-5} pptv·s^{-1}, and 2.6×10^{-3} pptv·s^{-1}, respectively. The median value of P_{extra} is 2.0×10^{-2} pptv·s^{-1}, about 79% of HONO daytime production budget of 2.5×10^{-2} pptv·s^{-1} in island-influenced air. While $P^*_{pNO_3\rightarrow HONO}$ (i.e., the upper limit estimate of HONO production rate via pNO$_3$ photolysis) accounts for ~79% of HONO production in clean marine air, it accounts for less than 10% in the island-influenced air masses. The remaining imbalances in the HONO budgets suggest that there existed other mechanisms that were important in the formation of HONO during the day.

In air masses in contact with the island surface, ground-related processes might play major roles in the daytime production of HONO. Heterogeneous NO$_2$ reaction on island surfaces (forest, buildings, and forest) via reaction (3) leads to HONO formation ($P_{NO_2(gound)\rightarrow HONO}$):

$$P_{NO_2(gound)\rightarrow HONO} = k_{NO_2-ground} \times [NO_2] \tag{14}$$

where $k_{NO_2-ground}$ is the rate constant for NO$_2$ to HONO conversions via reaction (3):

$$k_{NO_2-ground} = \frac{1}{4} \times \overline{v_{NO_2}} \times \frac{S}{V} \times \gamma_{NO_2-ground} \tag{15}$$

A $\frac{S}{V}$ value of 0.017 m^{-1} was calculated with an effective surface area of 2 m^2 per geometric surface area and an air column height (H) of 116 m. The value of H was calculated following Zhang et al. (2009) assuming a turbulent diffusion coefficient K_z of 10^5 cm^2 s^{-1}, and a HONO photolytic lifetime of 670 s (11 min). $\gamma_{NO_2-ground}$ is set as 2×10^{-5}, which is a upper-limit value suggested by Stemmler et al. (2006) taking into account potential photo-enhancement. The calculated median of $P_{NO_2-ground}$ in island-influenced air is 7.0×10^{-3} pptv·s^{-1} and accounts for 28% of the daytime HONO production budget in island-influenced air masses. Fig. 7 illustrates the contributions of different production and loss pathways in the daytime HONO budget from 10:00 to 15:00 in island-influenced air. $P_{NO_2(aerosol)\rightarrow HONO}$ contributes to <0.1% of the HONO production budget, and therefore is not displayed in Fig.7. The combined HONO production ($P_{NO+OH\rightarrow HONO} + P_{NO_2(gound)\rightarrow HONO} + P^*_{pNO_3\rightarrow HONO}$) accounts for only ~$1.2\times10^{-2}$ pptv·s^{-1} or ~48% of HONO production rate needed to compensate the HONO loss rate of ~2.5×10^{-2} pptv s^{-1} (Figure 7).
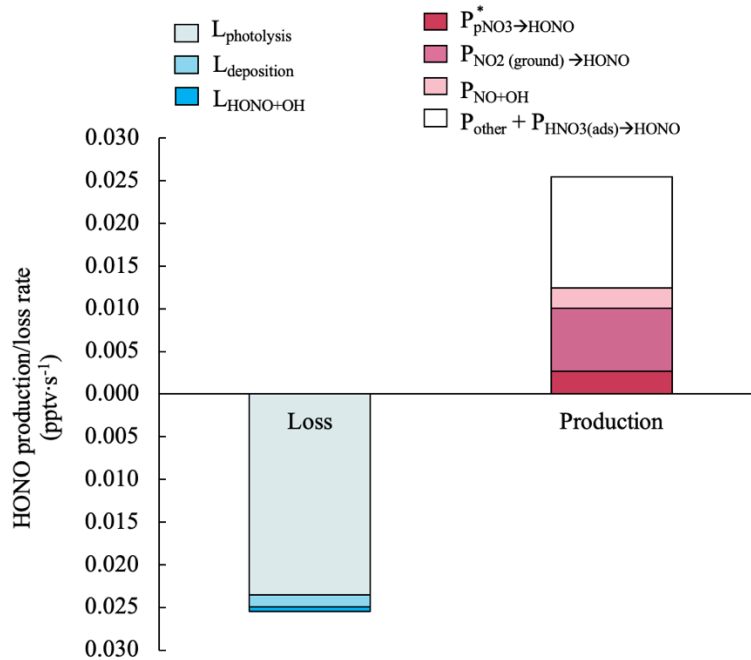
Figure 7: Median values for the production and loss rates of HONO contributed by different processes in island-influenced air masses from 10:00 to 15:00. HONO production rate by NO_2 heterogeneous reactions on aerosols contributed to <0.1% of the HONO production budget, and therefore is not displayed in this figure.

The HONO production rate unaccounted by NO_x-related processes and pNO_3 photolysis is calculated as:

$$P^*_{unaccounted} = L_{HONO} - P_{NO+OH \to HONO} - P_{NO_{2(aerosol)} \to HONO} -$$

$$-P_{NO_{2(ground)} \to HONO} - P^*_{pNO_3 \to HONO} \tag{16}$$

The calculated $P^*_{unaccounted}$ was used in our estimation for the noontime HONO concentration that cannot be explained by NO_x-related reactions and pNO_3 photolysis ($[HONO]_{unaccounted}$):

$$[HONO]_{unaccounted} = \frac{P^*_{unaccounted}}{J_{HONO} + k_{HONO+OH} \times [OH] + \frac{v_{HONO}}{H}} \tag{17}$$

It is possible that a significant fraction of $[HONO]_{unaccounted}$ could be explained by photolysis of nitric acid/nitrate adsorbed ($HNO_{3(ads)}$) on surfaces (e.g., the forest canopy). As suggested by previous field observations conducted in forested, rural area of North Michigan (Zhou et al., 2011) and Northeastern New York (Zhou et al., 2003, 2007), $HNO_{3(ads)}$ photolysis played a dominant role as HONO daytime source in low-NO_x environment. In this field study, island-modified air masses may interact with the island surfaces, especially the forest surfaces that half surrounds the sampling site at Tudor Hill. In the high-NO_x plumes, NO_x should be the dominant HONO precursor via reactions (R2) and (R3). However, these high-NO_x plumes picked up pollutants at point sources, such as power plant and cruise ships, and from small high traffic areas, such as

city of Hamilton, and only accounted for small fraction of air masses modified by the island. For the majority of the island-influenced air masses, NO_x concentration was relatively low ($\leq$ 1 ppbv), and the photolysis of nitric acid/nitrate adsorbed ($HNO_{3(ads)}$) on island surfaces may be an important HONO source, resulting in higher HONO/NO_x ratios than those observed in high-NO_x polluted plumes.

610   When $[HONO]_{unaccounted}$ is plotted against the averaged HNO_3 concentration over the prior 24 h ($[HNO_3]_{ave}$, a proxy for $HNO_{3(ads)}$ loading on the island surfaces), a significant and positive correlation is found ($R^2 = 0.50$, Fig. 8), suggesting that $HNO_{3(ads)}$ is likely an important precursor of HONO during the daytime. The nitric acid photolysis on surface could potentially contribute to a significant portion of the remaining HONO daytime production budget (i.e., $\sim 1.3 \times 10^{-2}$ pptv$\cdot$s^{-1}) that are not accounted for by the contributions from NO_x-related
615   reactions and pNO_3 photolysis in island-influenced air masses.
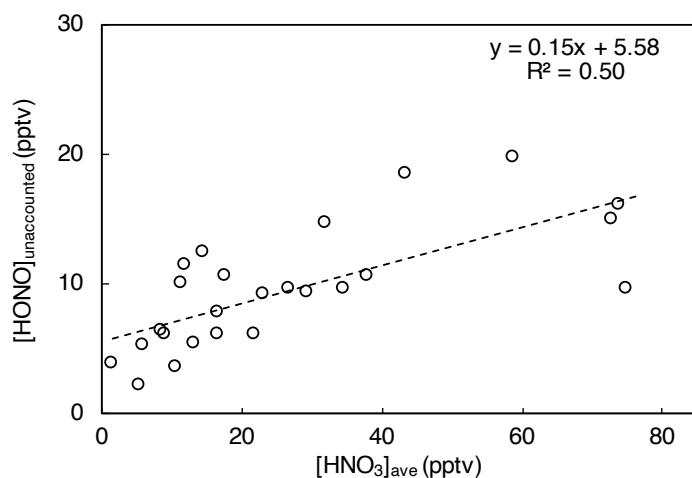
Figure 8: HONO concentration unaccounted by NO_x-related processes and pNO_3 photolysis ($[HONO]_{unaccounted}$, pptv, averaged for each day from 10:00 to 15:00) plotted against HNO_3 concentration averaged for 24 h prior to local noontime ($[HNO_3]_{ave}$, pptv) in island-influenced air with $[NO_2]$ < 1 ppbv

620

3.5 Case studies

Two case studies are presented here to show how the temporal variations in HONO can be caused by the various factors discussed in the previous sections:

Fig. 9 displayed a case study illustrating the temporal variations of HONO in response to various types of local
625   influences during the period of May 10–12. From the midnight of May 10 to 18:00 on May 11, the site was dominated by local winds from the east and was thus under the island influence. The observed NO_x levels were sensitive to wind direction, higher in air masses from the northeastern quarter with a power plant, major roads, and population centers, and lower in air masses from southeastern quarters. In polluted plumes (highlighted in blue), average NO_x concentration was 9 ppbv and the highest value reached 27 ppbv; the elevated NO_x levels
630   were associated with scavenging of O_3. The HONO concentration in these high-NO_x plumes also reached the

highest of 63 pptv in the selected period. Average HONO/NO_x ratio was 0.6% and 0.7% in the high-NO_x plumes before midnight and around sunrise of 5/11, respectively. These Low HONO/NO_x ratios were close to the published emission HONO/NO_x ratio of 0.79% (Liu et al., 2019), suggesting that direct anthropogenic emission was the dominant HONO source within the nighttime plume. It is interesting to point out that similar HONO/NO_x ratios were also observed in the smaller plume observed around 9:00 am on 5/11, despite significant HONO photolytic loss during the air mass transport, indicating the photochemical enhancement in HONO formation from reactions (2) – (5). During the after-midnight hours (0:30–5:00) of May 11, the NO_x level was low, with an average of 62 pptv, due to the lack of active emission sources. However, the HONO level (5–15 pptv) and HONO/NO_2 ratio (~0.10) were higher than their typical nighttime values in the clean marine air, probably due to the delayed release of HONO from heterogeneous NO_2 reaction occurred on island surfaces during high-NO_2 period a few hours earlier. From 18:00 on May 11 to the end of the selected period, the local wind shifted to the southwesterly and westerly, and the site started receiving marine air without modification by the island, with low HONO and NO_x levels most of the time. There was a short period (highlighted in pink) showing elevated NO_x attributed to ship emission but no HONO spike, suggesting the NO_x-related reactions was not a major HONO source in the marine air without interacting with the island, likely due to the limited surface area for heterogeneous NO_2 reactions in air masses over the ocean. The noontime HONO/NO_2 ratios (~0.04 on May 12) that were higher than those in polluted plumes (<0.012) support the argument that the photolysis of pNO_3 (R5) was the main contributor to the daytime formation of HONO in clean marine air. The highest HONO/NO_2 ratios (~0.13) were observed near the solar noon of the island-influenced period from May 10–11, reflecting active photochemical formation of HONO contributed via multiple mechanisms, including homogeneous and heterogeneous NO_x reactions (R2) and (R3), and the photolysis pNO_3 associated with aerosols (R5) and HNO_3 on the island surfaces (R4).
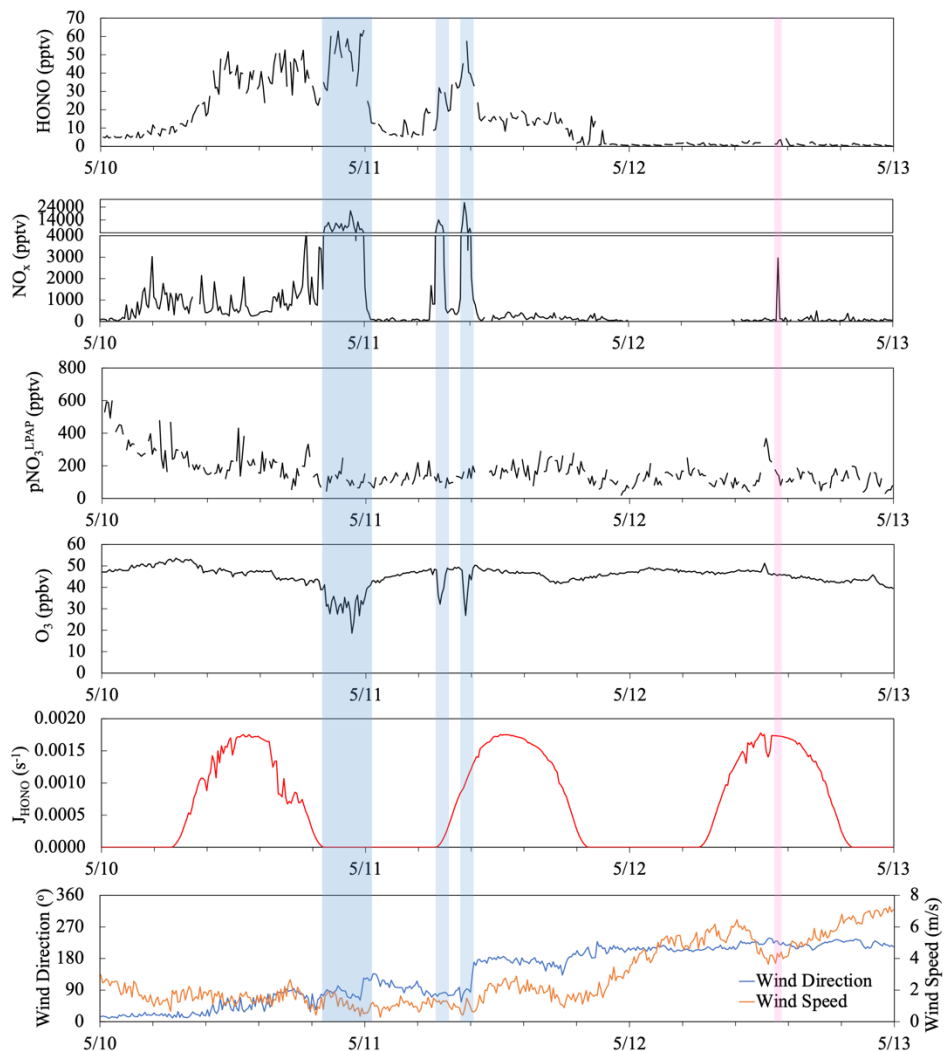
Figure 9: Time series plots of HONO, NO_x, pNO$_3^{LPAP}$, O_3, HONO photolysis rate constant (J_{HONO}), wind direction and wind speed from May 10 to 12, 2019. The light blue boxes highlighted highly polluted periods when the Tudor Hill site received urban pollutants. The pink box highlighted a short-term pollution plume resulted from ship emissions.

Fig. 10 depicted a case study showing the impact of long-range air mass transport on the temporal distribution of reactive nitrogen species. During the selected period from September 7–9, the site was dominated by the westerly flows (180° < wind direction < 360°) and thus the sampling site received mostly the clean marine air. There was only one short period near 8:00 on September 8 (highlighted in yellow) showing elevated HONO and NO_x concentrations attributed to the local emissions and island surface effect when local wind direction shifted briefly to the southeasterly. There were also a few spikes in NO_x emitted from ships in the upwind sea-lanes on September 8 and 9, but no HONO spikes due to the low surface area available for heterogeneous NO_2 reactions in this air mass traveling over the ocean. During the summer field campaign, the air mass traveled to the

THMAO site was dominated by well-aged marine air above the Atlantic Ocean. Starting from the early afternoon of September 7, hurricane Dorian disturbed the Bermuda high when it traveled along the eastern coast

670 of North America; the modeled backward trajectories indicate that the air mass arriving at the site during the period originated from the Northeastern US. The fast-traveling air flow from North America contained elevated levels of particulate nitrate (219– 585 pptv) and O_3 (29 – 49 ppbv) than those in aged marine air (average concentration for pNO$_3$^{LPAP} and O_3 were 127 pptv and 16 ppbv, respectively). During the air mass transition, we observed a strong increasing trend in HONO and HNO$_3$ concentrations from the evening of September 7 to the

675 early morning of September 8. The rapid increase in HNO$_3$ concentrations (from ~7 to 110 pptv) during a 24-h period from 8:00 on September 7 to 8:00 on September 8 largely affected the partitioning of nitrate between the gas phase and the aerosol phase (HNO$_3$/pNO$_3$ increased from 4% to 25%). An elevated daytime maximum in HONO concentration was found on September 8 (~6 pptv, three times higher than the ~2 pptv daytime HONO maximum on September 7). The photoproduction efficiency of HONO from aerosols also changed; the average

680 value of $J_{pNO_3}^{N}$ determined for aerosol samples collected on September 8 was $1.0\times10^{-5}\,s^{-1}$, much higher than the summer average value of $J_{pNO_3}^{N}$ (i.e., $3.4\times10^{-6}\,s^{-1}$). The HONO production efficiency from pNO$_3$ photolysis appears to be enhanced by the acidity of the aerosols.
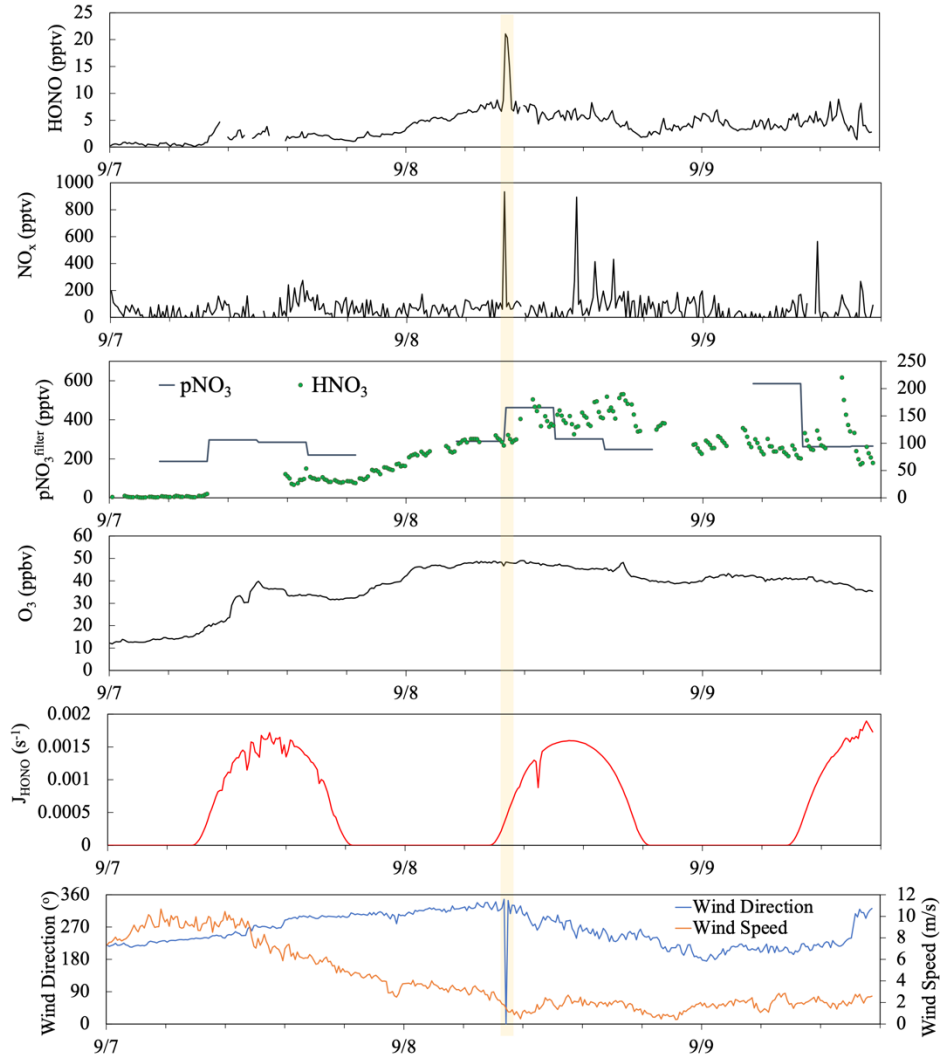
Figure 10: Time series plots of HONO, NO_x, pNO_3^{filter}, HNO_3, O_3, HONO photolysis rate constant (J_{HONO}), wind direction and wind speed from September 7 to 9, 2019. The yellow box highlighted short-term pollution plume resulted from a sudden shift in local wind direction.

4 Conclusions

Large temporal variations in HONO concentrations were observed at THMAO site in Bermuda during the spring and the summer of 2019, depending on the types of marine air masses and how the air masses interacting with the island. High concentrations of HONO, up to 278 pptv, were found in the locally emitted high-NO_x plumes. A HONO/NO_x ratio of 0.092 is derived from the HONO-NO_x correlation in the daytime high-NO_x plumes and is used to estimate the HONO source strength from NO_x-related reactions during the day. HONO concentrations were in low pptv and ten pptv levels in the low-NO_x marine air masses without and with island modification, respectively. Distinctive diurnal HONO variations were observed in both low-NO_x marine air with or without island modification, with daytime plateaus and nighttime valleys. Such diurnal variation patterns suggest that HONO was produced by photochemical processes during the day and that ocean surface was likely a net HONO sink. The photolysis of pNO_3, if moderately enhanced relative to HNO_3 photolysis by a factor of 29, can explain the missing daytime HONO source after counting the contribution from NO_x-related reactions in the clean marine air mass. The missing daytime HONO source accounts for the majority (~79%) of the overall daytime HONO budget of ~4.2×10^{-3} pptv·s^{-1} in clean marine air. To sustain the observed daytime HONO concentration in the low-NO_x island-modified air mass, a large HONO source, ~1.3×10^{-2} pptv·s^{-1}, is required, in addition to the known HONO production sources from NO_x and pNO_3 precursors, 9.7×10^{-3} pptv·s^{-1} and 2.6×10^{-3} pptv·s^{-1}, respectively. It is likely that the photolysis of $HNO_{3(ads)}$ on forest canopy and other island surfaces contribute significantly to this large missing HONO source in the low-NO_x island-modified air mass. The concentrations of HONO and its precursors, NO_x and pNO_3, were higher in spring than in summer in the clean marine air masses, attributed to the fact that the air masses arriving at the site in the summer had circulated over the North Atlantic Ocean and were more aged than the air masses that traveled from the North American continent in the spring. The "background" concentrations of HONO precursors decreased as the air masses aged and thereby lowered the production rates of HONO.

5 Author Contribution

XZ and YE designed the study. YZ, YW and XZ performed the development, calibration, and deployments of the reactive nitrogen measurements systems. XZ led the field campaigns. All authors contributed to the data collections during the field campaigns. YZ conducted the photochemistry experiments, performed the data processing, and prepared the manuscript with inputs from all coauthors.

6 Data Availability

Data are available upon request via xianliang.zhou@health.ny.gov.

7 Competing Interests

The authors declare no conflicts of interests.

8 Acknowledgment

This research is supported by the National Science Foundation's Atmospheric Chemistry Program and Chemical Oceanography Program through the grants AGS-1826989 (Xianliang Zhou), AGS-1826956 (Yasin Elshorbany), OCE-1829686 (Andrew Peters), and by Chinese National Natural Science Foundation through the grant 41875151 (Chunxiang Ye). We thank Dr. Haider Khwaja and lab members at Wadsworth Center for providing instrumentation and laboratory supports.

References

Acker, K., Febo, A., Trick, S., Perrino, C., Bruno, P., Wiesen, P., Möller, D., Wieprecht, W., Auel, R., Giusto, M., Geyer, A., Platt, U. and Allegrini, I.: Nitrous acid in the urban area of Rome, Atmos. Environ., 40(17), 3123–3133, doi:10.1016/j.atmosenv.2006.01.028, 2006a.

Acker, K., Möller, D., Wieprecht, W., Meixner, F. X., Bohn, B., Gilge, S., Plass-Dülmer, C. and Berresheim, H.: Strong daytime production of OH from HNO_2 at a rural mountain site, Geophys. Res. Lett., 33(2), L02809, doi:10.1029/2005GL024643, 2006b.

Atkinson, R., Baulch, D. L., Cox, R. A., Crowley, J. N., Hampson, R. F., Hynes, R. G., Jenkin, M. E., Rossi, M. J. and Troe, J.: Evaluated kinetic and photochemical data for atmospheric chemistry: Volume I - gas phase reactions of O_x, HO_x, NO_x and SO_x species, Atmos. Chem. Phys., 4(6), 1461–1738, doi:10.5194/acp-4-1461-2004, 2004.

Bao, F., Li, M., Zhang, Y., Chen, C. and Zhao, J.: Photochemical aging of Beijing urban PM2.5: HONO production, Environ. Sci. Technol., 52(11), 6309–6316, doi:10.1021/acs.est.8b00538, 2018.

Carr, S., Heard, D. E. and Blitz, M. A.: Comment on "Atmospheric Hydroxyl Radical Production from Electronically Excited NO_2 and H_2O," Science, 324(5925), 336b, doi:10.1126/science.1166669, 2009.

Carslaw, D. C. and Ropkins, K.: openair — An R package for air quality data analysis, Environ. Model. Softw., 27–28, 52–61, doi:10.1016/j.envsoft.2011.09.008, 2012.

Crilley, L. R., Kramer, L. J., Pope, F. D., Reed, C., Lee, J. D., Carpenter, L. J., Hollis, L. D. J., Ball, S. M. and Bloss, W. J.: Is the ocean surface a source of nitrous acid (HONO) in the marine boundary layer?, Atmos. Chem. Phys., 21(24), 18213–18225, doi:10.5194/acp-21-18213-2021, 2021.

Elshorbany, Y. F., Kurtenbach, R., Wiesen, P., Lissi, E., Rubio, M., Villena, G., Gramsch, E., Rickard, A. R., Pilling, M. J. and Kleffmann, J.: Oxidation capacity of the city air of Santiago, Chile, Atmos. Chem. Phys., 9(6), 2257–2273, doi:10.5194/acp-9-2257-2009, 2009.

Elshorbany, Y. F., Kleffmann, J., Kurtenbach, R., Lissi, E., Rubio, M., Villena, G., Gramsch, E., Rickard, A. R., Pilling, M. J. and Wiesen, P.: Seasonal dependence of the oxidation capacity of the city of Santiago de Chile, Atmos. Environ., 44(40), 5383–5394, doi:10.1016/j.atmosenv.2009.08.036, 2010.

Elshorbany, Y. F., Steil, B., Brühl, C. and Lelieveld, J.: Impact of HONO on global atmospheric chemistry calculated with an empirical parameterization in the EMAC model, Atmos. Chem. Phys., 12(20), 9977–10000,

755   doi:10.5194/acp-12-9977-2012, 2012.

Finlayson-Pitts, B. J., Wingen, L. M., Sumner, A. L., Syomin, D. and Ramazan, K. A.: The heterogeneous hydrolysis of NO_2 in laboratory systems and in outdoor and indoor atmospheres: An integrated mechanism, Phys. Chem. Chem. Phys., 5(2), 223–242, doi:10.1039/B208564J, 2003.

George, C., Strekowski, R. S., Kleffmann, J., Stemmler, K. and Ammann, M.: Photoenhanced uptake of gaseous
760   NO_2 on solid organic compounds: a photochemical source of HONO?, Faraday Discuss., 130, 195–210, doi:10.1039/B417888M, 2005.

Harrison, R. M., Peak, J. D. and Collins, G. M.: Tropospheric cycle of nitrous acid, J. Geophys. Res. Atmos., 101(D9), 14429–14439, doi:10.1029/96JD00341, 1996.

He, Y., Zhou, X., Hou, J., Gao, H. and Bertman, S. B.: Importance of dew in controlling the air-surface exchange of
765   HONO in rural forested environments, Geophys. Res. Lett., 33(2), L02813, doi:10.1029/2005GL024348, 2006.

Kasibhatla, P., Sherwen, T., Evans, M. J., Carpenter, L. J., Reed, C., Alexander, B., Chen, Q., Sulprizio, M. P., Lee, J. D., Read, K. A., Bloss, W., Crilley, L. R., Keene, W. C., Pszenny, A. A. P. and Hodzic, A.: Global impact of nitrate photolysis in sea-salt aerosol on NO_x, OH, and O_3 in the marine boundary layer, Atmos. Chem. Phys., 18(15), 11185–11203, doi:10.5194/acp-18-11185-2018, 2018.

770   Keene, W. C., Maring, H., Maben, J. R., Kieber, D. J., Pszenny, A. A. P., Dahl, E. E., Izaguirre, M. A., Davis, A. J., Long, M. S., Zhou, X., Smoydzin, L. and Sander, R.: Chemical and physical characteristics of nascent aerosols produced by bursting bubbles at a model air-sea interface, J. Geophys. Res. Atmos., 112(D21), D21202, doi:/10.1029/2007JD008464, 2007.

Kleffmann, J.: Daytime Sources of Nitrous Acid (HONO) in the Atmospheric Boundary Layer, ChemPhysChem,
775   8(8), 1137–1144, doi:10.1002/cphc.200700016, 2007.

Kleffmann, J., Becker, K. H. and Wiesen, P.: Heterogeneous NO_2 conversion processes on acid surfaces: possible atmospheric implications, Atmos. Environ., 32(16), 2721–2729, doi:10.1016/S1352-2310(98)00065-X, 1998.

Kleffmann, J., Becker, K. H., Lackhoff, M. and Wiesen, P.: Heterogeneous conversion of NO_2 on carbonaceous surfaces, Phys. Chem. Chem. Phys., 1(24), 5443–5450, doi:10.1039/A905545B, 1999.

780   Kleffmann, J., Kurtenbach, R., Lörzer, J., Wiesen, P., Kalthoff, N., Vogel, B. and Vogel, H.: Measured and simulated vertical profiles of nitrous acid—Part I: Field measurements, Atmos. Environ., 37(21), 2949–2955, doi:10.1016/S1352-2310(03)00242-5, 2003.

Kleffmann, J., Gavriloaiei, T., Hofzumahaus, A., Holland, F., Koppmann, R., Rupp, L., Schlosser, E., Siese, M. and Wahner, A.: Daytime formation of nitrous acid: A major source of OH radicals in a forest, Geophys. Res. Lett.,
785   32(5), L05818, doi:10.1029/2005GL022524, 2005.

Li, G., Lei, W., Zavala, M., Volkamer, R., Dusanter, S., Stevens, P. and Molina, L. T.: Impacts of HONO sources on the photochemistry in Mexico City during the MCMA-2006/MILAGO Campaign, Atmos. Chem. Phys., 10(14),

6551–6567, doi:10.5194/acp-10-6551-2010, 2010.

Li, S., Matthews, J. and Sinha, A.: Atmospheric Hydroxyl Radical Production from Electronically Excited NO_2 and
790   H_2O, Science, 319(5870), 1657–1660, doi:10.1126/science.1151443, 2008.

Li, X., Rohrer, F., Hofzumahaus, A., Brauers, T., Häseler, R., Bohn, B., Broch, S., Fuchs, H., Gomm, S., Holland,
F., Jäger, J., Kaiser, J., Keutsch, F. N., Lohse, I., Lu, K., Tillmann, R., Wegener, R., Wolfe, G. M., Mentel, T. F.,
Kiendler-Scharr, A. and Wahner, A.: Missing Gas-Phase Source of HONO Inferred from Zeppelin Measurements in
the Troposphere, Science, 344(6181), 292–296, doi:10.1126/science.1248999, 2014.

795   Li, Y. Q., Schwab, J. J. and Demerjian, K. L.: Fast time response measurements of gaseous nitrous acid using a
tunable diode laser absorption spectrometer: HONO emission source from vehicle exhausts, Geophys. Res. Lett.,
35(4), L04803, doi:10.1029/2007GL031218, 2008.

Liu, Y. , Nie, W. , Xu, Z. , Wang, T. , & Ding, A.: Semi-quantitative understanding of source contribution to nitrous
acid (HONO) based on 1 year of continuous observation at the sorpes station in eastern china, Atmospheric
800   Chemistry and Physics, 19(20), 13289-13308, doi:, 10.5194/acp-19-13289-2019, 2019.

Moody, J. L. and Galloway, J. N.: Quantifying the relationship between atmospheric transport and the chemical
composition of precipitation on Bermuda, Tellus B, 40B(5), 463–479, doi:10.1111/j.1600-0889.1988.tb00117.x,
1988.

Neftel, A., Blatter, A., Hesterberg, R. and Staffelbach, T.: Measurements of concentration gradients of HNO2 and
805   HNO3 over a semi-natural ecosystem, Atmos. Environ., 30(17), 3017–3025, doi:10.1016/1352-2310(96)00011-8,
1996.

Oswald, R., Behrendt, T., Ermel, M., Wu, D., Su, H., Cheng, Y., Breuninger, C., Moravek, A., Mougin, E., Delon,
C., Loubet, B., Pommerening-Röser, A., Sörgel, M., Pöschl, U., Hoffmann, T., Andreae, M. O., Meixner, F. X. and
Trebs, I.: HONO Emissions from Soil Bacteria as a Major Source of Atmospheric Reactive Nitrogen, Science,
810   341(6151), 1233–1235, doi:10.1126/science.1242266, 2013.

Oswald, R., Ermel, M., Hens, K., Novelli, A., Ouwersloot, H. G., Paasonen, P., Petäjä, T., Sipilä, M., Keronen, P.,
Bäck, J., Königstedt, R., Hosaynali Beygi, Z., Fischer, H., Bohn, B., Kubistin, D., Harder, H., Martinez, M.,
Williams, J., Hoffmann, T., Trebs, I. and Sörgel, M.: A comparison of HONO budgets for two measurement heights
at a field station within the boreal forest in Finland, Atmos. Chem. Phys., 15(2), 799–813, doi:10.5194/acp-15-799-
815   2015, 2015.

Perner, D. and Platt, U.: Detection of nitrous acid in the atmosphere by differential optical absorption, Geophys.
Res. Lett., 6(12), 917–920, doi:10.1029/GL006i012p00917, 1979.

Ramazan, K. A., Syomin, D. and Finlayson-Pitts, B. J.: The photochemical production of HONO during the
heterogeneous hydrolysis of NO_2, Phys. Chem. Chem. Phys., 6(14), 3836–3843, doi:10.1039/B402195A, 2004.

820   Reed, C., Evans, M. J., Crilley, L. R., Bloss, W. J., Sherwen, T., Read, K. A., Lee, J. D. and Carpenter, L. J.:
Evidence for renoxification in the tropical marine boundary layer, Atmos. Chem. Phys., 17(6), 4081–4092,

doi:10.5194/acp-17-4081-2017, 2017.

Reisinger, A. R.: Observations of HNO_2 in the polluted winter atmosphere: possible heterogeneous production on aerosols, Atmos. Environ., 34(23), 3865–3874, doi:10.1016/S1352-2310(00)00179-5, 2000.

825   Romer, P. S., Wooldridge, P. J., Crounse, J. D., Kim, M. J., Wennberg, P. O., Dibb, J. E., Scheuer, E., Blake, D. R., Meinardi, S., Brosius, A. L., Thames, A. B., Miller, D. O., Brune, W. H., Hall, S. R., Ryerson, T. B. and Cohen, R. C.: Constraints on aerosol nitrate photolysis as a potential source of HONO and NO_x, Environ. Sci. Technol., 52(23), 13738–13746, doi:10.1021/acs.est.8b03861, 2018.

Shi, Q., Tao, Y., Krechmer, J. E., Heald, C. L., Murphy, J. G., Kroll, J. H. and Ye, Q.: Laboratory investigation of
830   renoxification from the photolysis of inorganic particulate nitrate, Environ. Sci. Technol., 55(2), 854–861, doi:10.1021/acs.est.0c06049, 2021.

Stemmler, K., Ammann, M., Donders, C., Kleffmann, J. and George, C.: Photosensitized reduction of nitrogen dioxide on humic acid as a source of nitrous acid, Nature, 440(7081), 195–198, doi:10.1038/nature04603, 2006.

Stemmler, K., Ndour, M., Elshorbany, Y., Kleffmann, J., D'Anna, B., George, C., Bohn, B. and Ammann, M.: Light
835   induced conversion of nitrogen dioxide into nitrous acid on submicron humic acid aerosol, Atmos. Chem. Phys., 7(16), 4237–4248, doi:10.5194/acp-7-4237-2007, 2007.

Stutz, J., Alicke, B. and Neftel, A.: Nitrous acid formation in the urban atmosphere: Gradient measurements of NO_2 and HONO over grass in Milan, Italy, J. Geophys. Res. Atmos., 107(D22), 8192, doi:10.1029/2001JD000390, 2002.

Su, H., Cheng, Y., Oswald, R., Behrendt, T., Trebs, I., Meixner, F. X., Andreae, M. O., Cheng, P., Zhang, Y. and
840   Pöschl, U.: Soil nitrite as a source of atmospheric HONO and OH radicals, Science, 333(6049), 1616–1618, doi:10.1126/science.1207687, 2011.

Todd, D. L., Keene, W. C., Moody, J. L., Maring, H. and Galloway, J. N.: Effects of wet deposition on optical properties of the atmosphere over Bermuda and Barbados, J. Geophys. Res. Atmos., 108(D3), 4099, doi:10.1029/2001JD001084, 2003.

845   Trentmann, J., Andreae, M. O. and Graf, H.-F.: Chemical processes in a young biomass-burning plume, J. Geophys. Res. Atmos., 108(D22), 4705, doi:10.1029/2003JD003732, 2003.

Villena, G., Kleffmann, J., Kurtenbach, R., Wiesen, P., Lissi, E., Rubio, M. A., Croxatto, G. and Rappenglück, B.: Vertical gradients of HONO, NO_x and O_3 in Santiago de Chile, Atmos. Environ., 45(23), 3867–3873, doi:10.1016/j.atmosenv.2011.01.073, 2011a.

850   Villena, G., Bejan, I., Kurtenbach, R., Wiesen, P. and Kleffmann, J.: Development of a new Long Path Absorption Photometer (LOPAP) instrument for the sensitive detection of NO_2 in the atmosphere, Atmos. Meas. Tech., 4(8), 1663–1676, doi:10.5194/amt-4-1663-2011, 2011b.

Vogel, B., Vogel, H., Kleffmann, J. and Kurtenbach, R.: Measured and simulated vertical profiles of nitrous acid— Part II. Model simulations and indications for a photolytic source, Atmos. Environ., 37(21), 2957–2966,

855   doi:10.1016/S1352-2310(03)00243-7, 2003.

Wen, L., Chen, T., Zheng, P., Wu, L., Wang, X., Mellouki, A., Xue, L. and Wang, W.: Nitrous acid in marine boundary layer over eastern Bohai Sea, China: Characteristics, sources, and implications, Sci. Total Environ., 670, 282–291, doi:10.1016/j.scitotenv.2019.03.225, 2019.

Wojtal, P., Halla, J. D. and McLaren, R.: Pseudo steady states of HONO measured in the nocturnal marine boundary
860   layer: a conceptual model for HONO formation on aqueous surfaces, Atmos. Chem. Phys., 11(7), 3243–3261, doi:10.5194/acp-11-3243-2011, 2011.

Wong, K. W., Oh, H.-J., Lefer, B. L., Rappenglück, B. and Stutz, J.: Vertical profiles of nitrous acid in the nocturnal urban atmosphere of Houston, TX, Atmos. Chem. Phys., 11(8), 3595–3609, doi:10.5194/acp-11-3595-2011, 2011.

Yang, J., Shen, H., Guo, M.-Z., Zhao, M., Jiang, Y., Chen, T., Liu, Y., Li, H., Zhu, Y., Meng, H., Wang, W. and
865   Xue, L.: Strong marine-derived nitrous acid (HONO) production observed in the coastal atmosphere of northern China, Atmos. Environ., 244, 117948, doi:10.1016/j.atmosenv.2020.117948, 2021.

Ye, C., Zhou, X., Pu, D., Stutz, J., Festa, J., Spolaor, M., Cantrell, C., Mauldin, R. L., Weinheimer, A. and Haggerty, J.: Comment on "Missing gas-phase source of HONO inferred from Zeppelin measurements in the troposphere," Science, 348(6241), 1326-d, doi:10.1126/science.aaa1992, 2015.

870   Ye, C., Gao, H., Zhang, N. and Zhou, X.: Photolysis of nitric acid and nitrate on natural and artificial surfaces, Environ. Sci. Technol., 50(7), 3530–3536, doi:10.1021/acs.est.5b05032, 2016a.

Ye, C., Zhou, X., Pu, D., Stutz, J., Festa, J., Spolaor, M., Tsai, C., Cantrell, C., Mauldin, R. L., Campos, T., Weinheimer, A., Hornbrook, R. S., Apel, E. C., Guenther, A., Kaser, L., Yuan, B., Karl, T., Haggerty, J., Hall, S., Ullmann, K., Smith, J. N., Ortega, J. and Knote, C.: Rapid cycling of reactive nitrogen in the marine boundary layer,
875   Nature, 532(7600), 489–491, doi:10.1038/nature17195, 2016b.

Ye, C., Heard, D. E. and Whalley, L. K.: Evaluation of novel routes for NO$_x$ formation in remote regions, Environ. Sci. Technol., 51(13), 7442–7449, doi:10.1021/acs.est.6b06441, 2017a.

Ye, C., Zhang, N., Gao, H. and Zhou, X.: Photolysis of particulate nitrate as a source of HONO and NO$_x$, Environ. Sci. Technol., 51(12), 6849–6856, doi:10.1021/acs.est.7b00387, 2017b.

880   Ye, C., Zhou, X., Pu, D., Stutz, J., Festa, J., Spolaor, M., Tsai, C., Cantrell, C., Mauldin III, R. L., Weinheimer, A., Hornbrook, R. S., Apel, E. C., Guenther, A., Kaser, L., Yuan, B., Karl, T., Haggerty, J., Hall, S., Ullmann, K., Smith, J. and Ortega, J.: Tropospheric HONO distribution and chemistry in the southeastern US, Atmos. Chem. Phys., 18(12), 9107–9120, doi:10.5194/acp-18-9107-2018, 2018.

Zabarnick, S.: Kinetics of the reaction OH + NO + M → HONO + M as a function of temperature and pressure in
885   the presence of argon, SF$_6$, and N$_2$ bath gas, Chem. Phys., 171(1), 265–273, doi:10.1016/0301-0104(93)85149-3, 1993.

Zha, Q., Xue, L., Wang, T., Xu, Z., Yeung, C., Louie, P. K. K. and Luk, C. W. Y.: Large conversion rates of NO$_2$ to

HNO$_2$ observed in air masses from the South China Sea: Evidence of strong production at sea surface?, Geophys. Res. Lett., 41(21), 7710–7715, doi:10.1002/2014GL061429, 2014.

890   Zhang, N., Zhou, X., Shepson, P. B., Gao, H., Alaghmand, M. and Stirm, B.: Aircraft measurement of HONO vertical profiles over a forested region, Geophys. Res. Lett., 36(15), L15820, doi:10.1029/2009GL038999, 2009.

Zhou, X., Beine, H. J., Honrath, R. E., Fuentes, J. D., Simpson, W., Shepson, P. B. and Bottenheim, J. W.: Snowpack photochemical production of HONO: A major source of OH in the Arctic boundary layer in springtime, Geophys. Res. Lett., 28(21), 4087–4090, doi:10.1029/2001GL013531, 2001.

895   Zhou, X., Civerolo, K., Dai, H., Huang, G., Schwab, J. and Demerjian, K.: Summertime nitrous acid chemistry in the atmospheric boundary layer at a rural site in New York State, J. Geophys. Res. Atmos., 107(D21), 4590, doi:10.1029/2001JD001539, 2002.

Zhou, X., Gao, H., He, Y., Huang, G., Bertman, S. B., Civerolo, K. and Schwab, J.: Nitric acid photolysis on surfaces in low-NOx environments: Significant atmospheric implications, Geophys. Res. Lett., 30(23), 2217,

900   doi:10.1029/2003GL018620, 2003.

Zhou, X., Huang, G., Civerolo, K., Roychowdhury, U. and Demerjian, K. L.: Summertime observations of HONO, HCHO, and O3 at the summit of Whiteface Mountain, New York, J. Geophys. Res. Atmos., 112(D8), D08311, doi:10.1029/2006JD007256, 2007.

Zhou, X., Zhang, N., TerAvest, M., Tang, D., Hou, J., Bertman, S., Alaghmand, M., Shepson, P. B., Carroll, M. A.,

905   Griffith, S., Dusanter, S. and Stevens, P. S.: Nitric acid photolysis on forest canopy surface as a source for tropospheric nitrous acid, Nat. Geosci., 4(7), 440–443, doi:10.1038/ngeo1164, 2011.